

LUDWIG-MAXIMILIANS-UNIVERSITÄT MÜNCHEN

**Development of a Laser-Cutting
Microscope and Analysis of Graphene
Ablation Process**

**Entwicklung eines Mikroskops für
Laserschneidprozesse und Untersuchung
der Graphenablation**

Bachelor's Thesis

by

Carlos Steiner Navarro

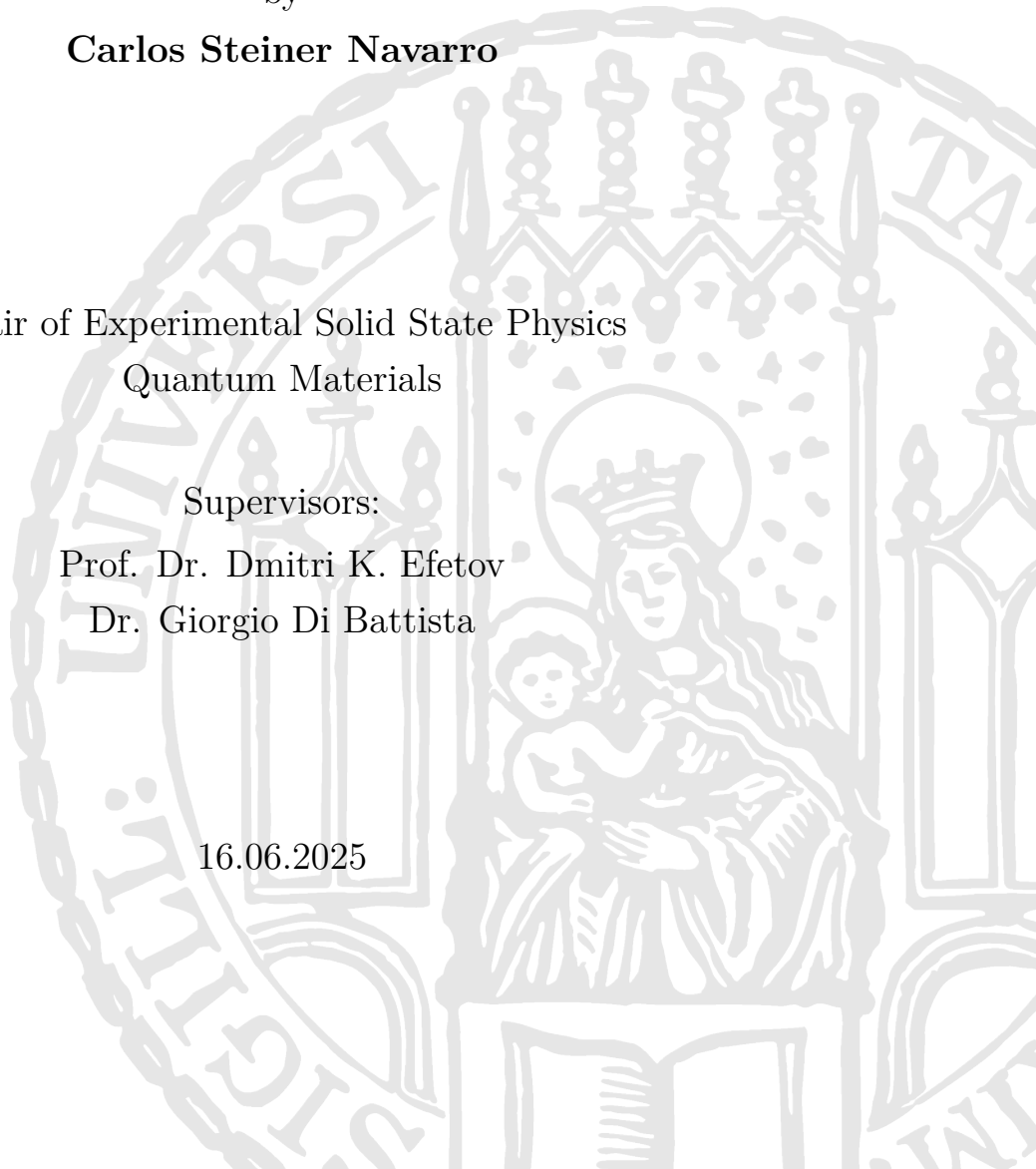
Chair of Experimental Solid State Physics
Quantum Materials

Supervisors:

Prof. Dr. Dmitri K. Efetov

Dr. Giorgio Di Battista

16.06.2025



Abstract

Graphene, a single atomic layer of carbon, exhibits extraordinary mechanical, electronic, and thermal properties, making it a model system for two-dimensional materials. When two graphene layers are stacked with a small twist angle, especially near 1.1° , strongly correlated phases such as superconductivity emerge, sparking intense research interest. Fabricating such twisted bilayer graphene devices requires precisely cutting monolayer flakes to maintain crystallographic alignment. Since mechanical cutting often introduces strain and defects, laser-based cutting offers a promising non-contact alternative for high-precision processing. In this work, a custom-built laser-cutting microscope was developed, integrating optical imaging, precise laser micromachining, and a Python-based control interface. Systematic experiments on single- and multilayer graphene revealed a decreasing damage threshold fluence with increasing layer number, governed by enhanced optical absorption and reduced in-plane thermal conductivity due to suppressed flexural phonon scattering. Additionally, prolonged irradiation exhibited a pronounced incubation effect, lowering the ablation threshold through cumulative heating. The system further allowed the investigation of cutting dynamics, showing that higher scanning speeds enable narrower, cleaner cuts approaching the diffraction limit. First experiments on hBN-encapsulated graphene indicated that while encapsulation initially protects the graphene, extended irradiation may lead to conductivity loss, likely via indirect structural degradation. The developed platform provides a versatile tool for both fabrication and detailed studies of laser-graphene interactions.

Acknowledgements

I would like to express my sincere and deepest gratitude to my supervisor, Dr. Giorgio Di Battista, for his continuous support, guidance, and motivation. His expertise, insightful feedback, immense patience, and constant helpfulness have greatly contributed to the successful completion of my thesis.

I extend my special thanks to all my colleagues from the Efetov Lab for their invaluable support, helpfulness, and insightful conversations. Engaging discussions — whether about physics or other topics — fostered a collaborative atmosphere that greatly enriched my experience. In particular, I would like to thank Leon Schubert and Leon Benoist for their enormous help throughout the thesis, as well as for kindly providing their samples, which allowed me to perform measurements and test the microscope.

I am equally grateful to Prof. Dr. Dmitri K. Efetov for granting me the opportunity to join the team and conduct my research in such a prestigious laboratory, surrounded by outstanding people. I am thankful for his guidance, interest, and continuous support throughout the development of my thesis, as well as for the invaluable scientific insights I gained during this time.

Finally, I would like to express my deepest appreciation to my parents, Christian and Consuelo, and closest family for their constant support, encouragement, care, and love, despite the distance throughout my studies and thesis work. I would also like to sincerely thank my high school teacher, Ernesto Civera, for nurturing my curiosity in physics and for his ongoing support.

Contents

1	Introduction and Motivation	3
2	Theoretical Background	7
2.1	Graphene	7
2.1.1	Twisted Bilayer Graphene	12
2.1.2	Graphene Laser Ablation	13
2.1.3	hBN-encapsulated Graphene	16
2.2	Optics	17
2.2.1	Laser	18
2.2.2	Microscope	19
2.2.3	Diffraction Limit	20
2.2.4	Dichroic mirror	21
2.2.5	Beam Collimator	21
2.3	Optical Contrast	21
3	Methods	25
3.1	Laser-Cutting Microscope	25
3.1.1	Building the Microscope	25
3.1.2	Building the Graphical User Interface (GUI)	29
3.2	Optical Microscopy	36
4	Results and Discussion	39
4.1	Damage-Threshold Graphene	39
4.1.1	Layer-Dependent Damage Threshold	39
4.1.2	Time-Dependent Damage Threshold	46
4.1.3	Analysis of Cuts	49
4.2	Cutting hBN-Encapsulated Graphene	50
5	Conclusions	55

A GUI Code Structure and Python Scripts	57
A.0.1 GUI Widgets	57
A.0.2 Software Modules	57
A.0.3 Python Script for Layer-Dependent Threshold	57
A.0.4 Python Script for Time-Dependent Threshold	60
A.0.5 Python Script for Graphene Cutting Characteristics	63
B Commands for Controlling Motors and Laser	65
C Measurements	67
C.1 Layer-dependent Damage Threshold	67
C.2 Time-Dependent Damage Threshold	67

Chapter 1

Introduction and Motivation

The discovery and isolation of graphene in 2004 marked the beginning of a new era in condensed matter physics, opening the way for the exploration of two-dimensional (2D) materials. These materials, consisting of single- or few-atom-thick layers, are held together by strong covalent or ionic bonds within the layers and weak van der Waals forces between them [1]. Their extreme thinness, often just one atom thick, gives rise to a range of extraordinary properties [2]. In the 2D limit, materials like graphene exhibit mechanical robustness, exceptional flexibility, and unique electrical, optical, and thermal characteristics that are often absent or significantly muted in their bulk counterparts [3].

Beyond these intrinsic properties, one of the most compelling aspects of 2D materials is their tunability. By stacking individual layers and rotating them with respect to each other, researchers can engineer new structures with emergent behaviors [4]. This has led to the emergence of the field known as *twistronics*, which studies how twisting 2D materials at precise angles affects their electronic properties. A particularly groundbreaking discovery in this field is the emergence of superconductivity and other exotic correlated phases when two graphene layers are stacked with a relative twist of approximately 1.1° , known as the *magic angle* [4]. At this angle, the resulting moiré superlattice modifies the electronic band structure, creating so-called flat bands in which the electrons are highly localized. This localization enhances electron-electron interactions, giving rise to phenomena such as superconductivity, correlated insulating states, and topological behaviors—all within a single, chemically unaltered material system [2].

However, realizing such twisted bilayer graphene devices, specifically Magic Angle Twisted Bilayer Graphene (MATBG), presents substantial fabrication challenges. The construction of these devices demands precise alignment of two monolayer graphene flakes, rotated by precisely 1.1° . To ensure crystallographic alignment, both layers need to originate from the same parent flake, ensuring identical lattice orientation and minimal lattice mismatch [5]. Consequently, a single monolayer graphene flake must be carefully cut into two parts. One half is then picked up and rotated before being stacked on the other. This cutting step is critical but delicate; mechanical cutting methods—such as using a cantilever tip to scratch and separate the flake—often introduce strain, irregular edge morphologies, and unintended tearing [5]. These imperfections not only complicate the subsequent stacking process

but also can degrade device performance.

To address these issues, laser-based cutting techniques have been used [6]. By focusing a laser beam onto the graphene surface, it is possible to locally sublime material along predefined paths, enabling clean, precise cuts with minimal mechanical stress. This method not only improves the quality of the edges but also allows for complex patterning of graphene flakes, preparing them for deterministic stacking with high precision. Developing a reliable, microscope-integrated laser-cutting system tailored for graphene manipulation is therefore a key step toward the reproducible fabrication of advanced 2D heterostructures and quantum devices [5].

To construct a microscope capable of laser-cutting graphene with high precision, several key physical and technical considerations must be addressed. From a physical standpoint, it is essential to reach the threshold temperature required for graphene sublimation. This necessitates delivering a sufficiently high pulse energy in an extremely short time interval—typically in the form of short laser pulses—to prevent unwanted thermal diffusion and relaxation into the surrounding substrate. Achieving this condition ensures localized heating and minimizes collateral damage.

The laser pulse must be tightly focused to a single, micron- or even submicron-sized spot on the graphene surface. The smaller the focal point, the higher the resulting fluence (energy per unit area), which directly contributes to the effectiveness and cleanliness of the cut [5]. A tightly confined beam not only concentrates energy but also allows for finer control over the cutting geometry, crucial for deterministic patterning and stacking.

Another important factor is the interaction between the laser and the graphene itself. Graphene’s optical absorption—particularly within the visible to near-infrared spectrum—determines how efficiently the pulse energy is absorbed and converted into heat [7]. Therefore, the choice of optical components must match both the laser source and the physical properties of graphene.

Several experiments have been conducted to investigate the laser-cutting behavior of both single-layer graphene (SLG) and multilayer graphene (MLG). These experiments explored critical parameters such as the role of the substrate, the influence of multi-pulse irradiation and thermal incubation on the fluence threshold [8], and how the addition of successive layers affects the energy required to initiate cutting [9].

This thesis presents the design and construction of a custom laser-cutting microscope and examines in detail the cutting dynamics of graphene. In particular, it investigates how the fluence threshold—the minimum energy density required to cut—depends on the number of graphene layers and the duration of laser exposure. Additionally, aspects such as the overall cut quality and the feasibility of cutting hBN-encapsulated graphene are also addressed.

The developed microscope combines high-resolution optical imaging with precise laser micromachining capabilities. It is supported by an intuitive Graphical User Interface (GUI) that enables real-time visualization and execution of custom cutting paths. This integration allows for flexible and user-friendly operation, facilitating both experimental studies and potential device fabrication.

The experimental results demonstrate that the fluence required to induce damage

in graphene decreases with the number of layers, up to a saturation point beyond which additional layers no longer significantly reduce the threshold. Furthermore, extended irradiation over multiple seconds was shown to effectively lower the fluence threshold due to cumulative heating effects. These findings provide valuable insight into the thermal and optical behavior of 2D materials under pulsed laser irradiation.

Throughout Chapter 2, a general introduction to graphene, including its fundamental properties and the physical conditions necessary for effective laser cutting is provided. It also introduces key concepts in optics that underpin the microscope's design and functionality. Chapter 3 details the construction process of the laser-cutting microscope, including the mechanical and optical components, as well as the development of the GUI for user interaction. Chapter 4 presents the experimental measurements and results, focusing on how layer number and irradiation time influence the fluence threshold. It also examines the correlation between cutting power, speed, and edge quality, and discusses the particular challenges and strategies associated with cutting hBN-encapsulated graphene.



Chapter 2

Theoretical Background

2.1 Graphene

Graphene is a two-dimensional (2D) allotrope of carbon consisting of a single atomic layer arranged in a hexagonal lattice [10]. It can be considered the fundamental building block of other carbon-based materials: it rolls into carbon nanotubes, folds into fullerenes, or stacks to form graphite. The discovery and isolation of graphene in 2004 marked a milestone in condensed matter physics due to its extraordinary electronic, mechanical, and thermal properties.

Each carbon atom in graphene contributes six electrons, which in the ground state occupy the electron configuration $1s^2 2s^2 2p_x^2 2p_y^2$. During the formation of chemical bonds in the planar structure of graphene, one of the 2s electrons is excited into the unoccupied $2p_z$ orbital [11]. This rearrangement facilitates the formation of three equivalent hybrid orbitals via the sp^2 hybridization process. Specifically, the 2s, $2p_x$, and $2p_y$ orbitals combine to form three sp^2 hybrid orbitals oriented 120° apart, lying in the same plane [12]. These orbitals form strong covalent σ -bonds with three adjacent carbon atoms, resulting in the characteristic honeycomb structure of graphene 2.1.

The fourth valence electron remains in the $2p_z$ orbital, which is perpendicular to the

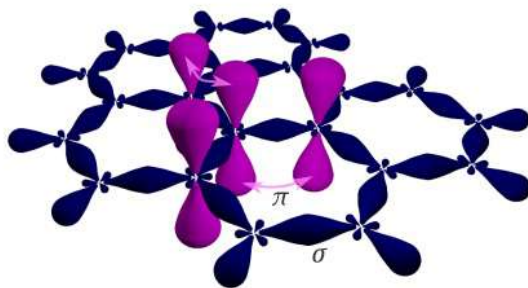


Figure 2.1: Atomic structure and electronic configuration of graphene. The carbon atoms form a hexagonal lattice with sp^2 hybridization, creating strong σ -bonds in-plane, while the remaining p_z orbitals contribute to the delocalized π -bond network responsible for graphene's unique electronic properties. Taken from Ref. [13].

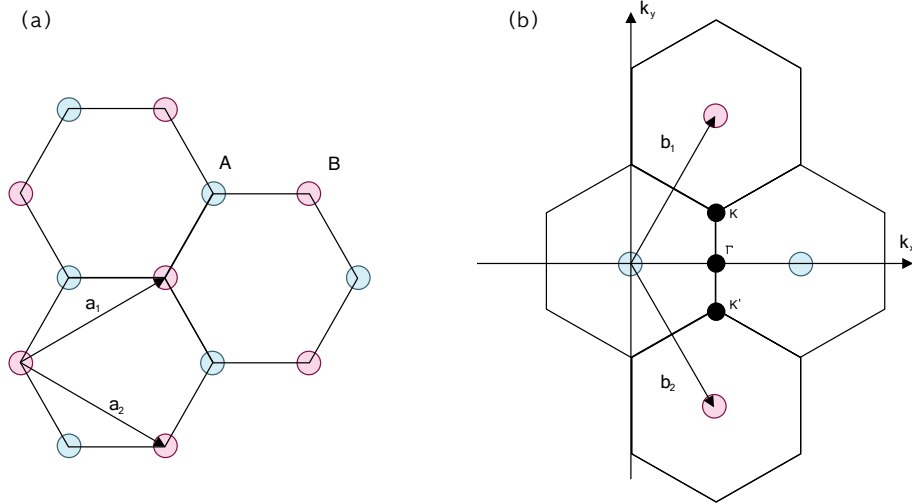


Figure 2.2: (a) Graphene's hexagonal lattice structure in real-space with unit vectors a_1 and a_2 . (b) Corresponding reciprocal lattice with vectors b_1 and b_2 , defining the Brillouin zone relevant for its electronic band structure. Adapted from Ref. [10].

graphene plane. This unhybridized orbital forms a delocalized π -bonding network through overlap with the $2p_z$ orbitals of neighboring carbon atoms. These π -bonds are responsible for many of graphene's unique electronic properties, including high electron mobility and the formation of Dirac cones in its electronic band structure [11] [12].

In graphite, which consists of stacked graphene layers, the weak van der Waals forces between adjacent layers result in relatively low interlayer binding energy. These interactions are mediated by the π -electrons residing in the $2p_z$ orbitals. Because π -bonding is much weaker than the in-plane σ -bonding, the layers can easily slide over one another, granting graphite its lubricating properties [11].

From a band theory perspective, the overlap of $2p_z$ orbitals leads to the formation of bonding and antibonding molecular orbitals, giving rise to the valence π -band and the conduction π^* -band, respectively. The continuous and delocalized nature of these bands allows electrons in graphene to behave as massless Dirac fermions under certain conditions [12, 14].

Calculation of Band Structure

The graphene unit cell comprises two equivalent hexagonal sublattices, A and B, which form a non-primitive unit cell [15]. The lattice vectors are:

$$\vec{a}_1 = \frac{\sqrt{3}a_0}{2} \begin{pmatrix} \sqrt{3} \\ -1 \end{pmatrix}, \quad \vec{a}_2 = \frac{\sqrt{3}a_0}{2} \begin{pmatrix} \sqrt{3} \\ 1 \end{pmatrix}, \quad (2.1)$$

where $a_0 = 0.142$ nm is the distance between two adjacent carbon atoms.

The Fourier transform of the Bravais lattice into momentum space (k -space) yields the Brillouin zone, which plays a fundamental role in the analysis of diffraction and

electron wave functions. The reciprocal lattice is spanned by the reciprocal vectors:

$$\vec{b}_1 = \frac{2\pi}{3a_0} \begin{pmatrix} 1 \\ -\sqrt{3} \end{pmatrix}, \quad \vec{b}_2 = \frac{2\pi}{3a_0} \begin{pmatrix} 1 \\ \sqrt{3} \end{pmatrix}. \quad (2.2)$$

The A and B sublattices correspond to the K and K' points in the Brillouin zone. The electronic band structure of graphene can be approximated using the tight-binding Hamiltonian considering only nearest-neighbor interactions [15]:

$$\hat{H}\psi_{\vec{k}}(\vec{r}) = \left[-\frac{\hbar^2}{2m}\nabla^2 + U(\vec{r}) \right] \psi_{\vec{k}}(\vec{r}) = E(\vec{k})\psi_{\vec{k}}(\vec{r}). \quad (2.3)$$

As the two sublattices A and B only commute separately with the Hamiltonian, their wavefunctions are treated independently:

$$\psi_{\vec{k}}(\vec{r}) = \psi_{\vec{k}A}(\vec{r}) + \psi_{\vec{k}B}(\vec{r}), \quad (2.4)$$

The solution of the Hamiltonian, with lattice vectors $\vec{R} = u\vec{a}_1 + v\vec{a}_2$, yields:

$$H_{AB} = \sum_n \int e^{i\vec{k}\cdot\vec{R}_n} u_A^*(\vec{r} - \vec{R}_n) H(\vec{r}) u_B(\vec{r} - \vec{R}_n) d\vec{r}. \quad (2.5)$$

Rewriting the wavefunction in spinor representation [15]:

$$\psi_{\vec{k}}(\vec{r}) = \begin{pmatrix} \psi_{\vec{k}A}(\vec{r}) \\ \psi_{\vec{k}B}(\vec{r}) \end{pmatrix}, \quad (2.6)$$

the Hamiltonian becomes:

$$H(\vec{k}) = \begin{bmatrix} H_{AA} & H_{AB} \\ H_{BA} & H_{BB} \end{bmatrix}, \quad (2.7)$$

where the diagonal terms representing self-energies become $H_{AA} = H_{BB} = 0$ by symmetry.

The off-diagonal terms H_{AB} and H_{BA} represent nearest-neighbor hopping, characterized by the vectors:

$$\vec{\delta}_1 = \frac{a_0}{2} \begin{pmatrix} 1 \\ -\sqrt{3} \end{pmatrix}, \quad \vec{\delta}_2 = \frac{a_0}{2} \begin{pmatrix} 1 \\ \sqrt{3} \end{pmatrix}, \quad \vec{\delta}_3 = a_0 \begin{pmatrix} -1 \\ 0 \end{pmatrix}, \quad (2.8)$$

which yield:

$$H_{AB} = \gamma_0 \sum_n e^{-i\vec{k}\cdot\vec{\delta}_n} = \gamma_0 \left[1 + e^{-i(\sqrt{3}k_x a_0/2 - k_y a_0/2)} + e^{-i(\sqrt{3}k_x a_0/2 + k_y a_0/2)} \right], \quad (2.9)$$

$$H_{BA} = \gamma_0 \sum_n e^{i\vec{k}\cdot\vec{\delta}_n} = \gamma_0 \left[1 + e^{i(\sqrt{3}k_x a_0/2 - k_y a_0/2)} + e^{i(\sqrt{3}k_x a_0/2 + k_y a_0/2)} \right], \quad (2.10)$$

where γ_0 is the hopping parameter:

$$\gamma_0 = \int u_A^*(\vec{r}) H(\vec{r}) u_B(\vec{r} + \vec{\delta}_3) \approx 2.8 \text{ eV}. \quad (2.11)$$

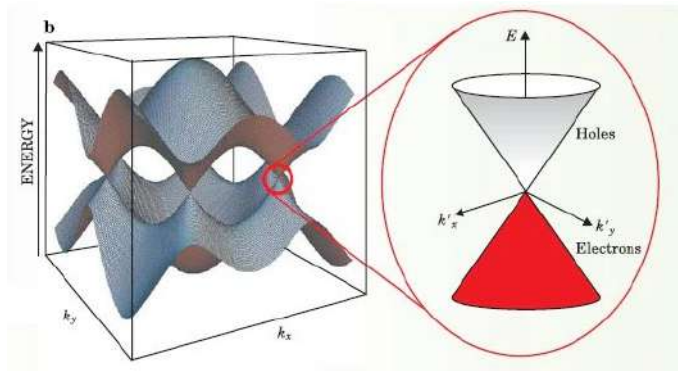


Figure 2.3: Calculated electronic band structure of monolayer graphene, showing the linear dispersion relation around the Dirac points. Taken from Ref. [16].

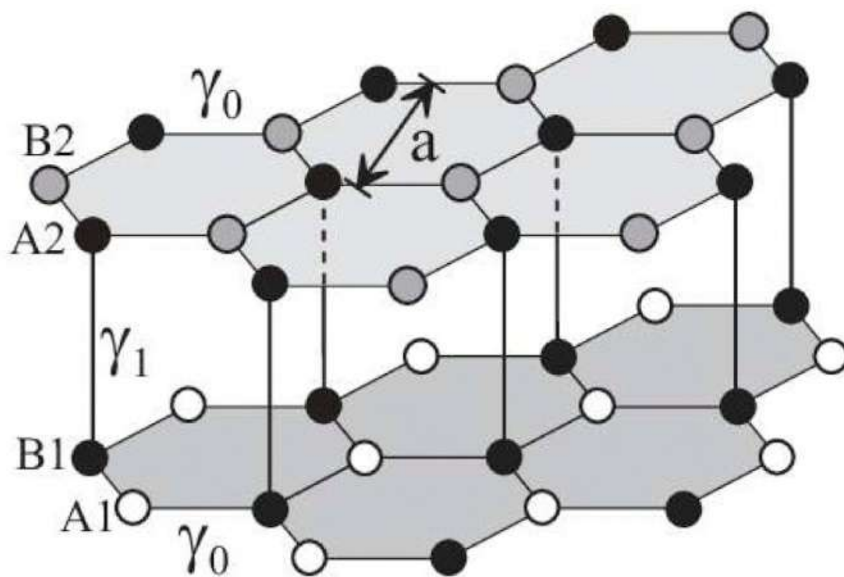


Figure 2.4: Atomic stacking configuration of bilayer graphene (AB stacking). Interlayer hopping parameters γ_0 and γ_1 describe the coupling between the two layers, which modifies its electronic band structure. Taken from Ref. [15].

Solving for the energy eigenvalues:

$$\begin{vmatrix} H_{AA} & H_{AB} \\ H_{BA} & H_{BB} \end{vmatrix} = 0 \quad (2.12)$$

yields:

$$E(\vec{k}) = \pm \gamma_0 \sqrt{1 + 4 \cos^2 \left(\frac{k_y a_0}{2} \right) + 4 \cos \left(\frac{\sqrt{3} k_x a_0}{2} \right) \cos \left(\frac{k_y a_0}{2} \right)}. \quad (2.13)$$

The positive eigenvalue corresponds to the conduction (π) band, the negative to the valence (π^*) band.

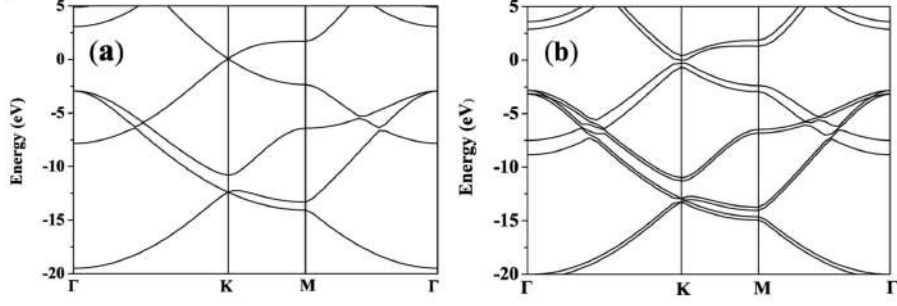


Figure 2.5: Comparison of band structures for monolayer (a) and bilayer (b) graphene. The bilayer structure exhibits additional conduction and valence bands due to interlayer coupling. Taken from Ref. [17].

Band Structure Calculation for Multilayer Graphene

The tight-binding model can be extended to multilayer graphene by incorporating interlayer hopping terms.

For AB-stacked bilayer graphene, the wavefunction is expanded as [15]:

$$\psi_{\vec{k}}(\vec{r}) = \begin{pmatrix} \psi_{\vec{k}A_1}(\vec{r}) \\ \psi_{\vec{k}B_1}(\vec{r}) \\ \psi_{\vec{k}A_2}(\vec{r}) \\ \psi_{\vec{k}B_2}(\vec{r}) \end{pmatrix}, \quad (2.14)$$

and only nearest-neighbor and interlayer hopping are considered. The interlayer hopping parameter is:

$$H_{B_1A_2} = \gamma_1. \quad (2.15)$$

Applying an interlayer potential Δ modifies self-energies:

$$-H_{A_1A_1} = -H_{B_1B_1} = H_{A_2A_2} = H_{B_2B_2} = \Delta/2. \quad (2.16)$$

Solving the eigenvalue equation for the full Hamiltonian:

$$\mathcal{H} = \begin{pmatrix} -\Delta/2 & \gamma_0 \sum_i e^{-i\vec{k}\cdot\vec{\delta}_i} & 0 & 0 \\ \gamma_0 \sum_i e^{-i\vec{k}\cdot\vec{\delta}_i} & -\Delta/2 & \gamma_1 & 0 \\ 0 & \gamma_1 & \Delta/2 & \gamma_0 \sum_i e^{-i\vec{k}\cdot\vec{\delta}_i} \\ 0 & 0 & \gamma_0 \sum_i e^{-i\vec{k}\cdot\vec{\delta}_i} & \Delta/2 \end{pmatrix} \quad (2.17)$$

leads to the bilayer band structure:

$$\epsilon_{1,2}^{\pm}(\vec{k}) = \pm \sqrt{\frac{\gamma_1^2}{2} + \frac{\Delta^2}{4} + \hbar^2 v_F^2 \kappa^2} \pm \sqrt{\frac{\gamma_1^4}{4} + \hbar^2 v_F^2 \kappa^2 (\gamma_1^2 + \Delta^2)}. \quad (2.18)$$

Therefore, adding more layers changes the core properties of graphene itself [18].

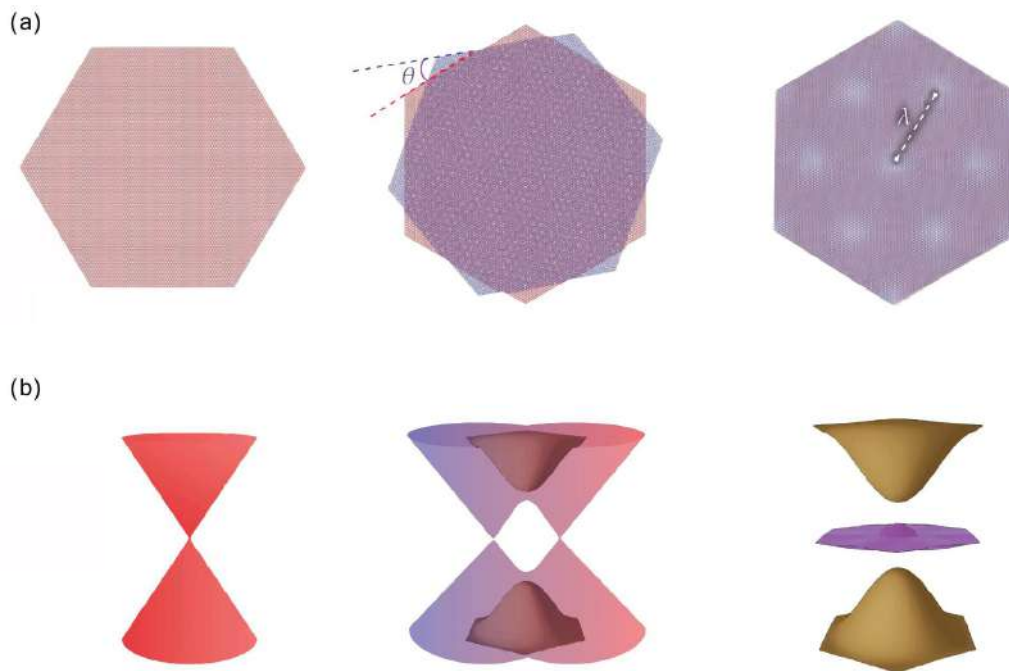


Figure 2.6: Illustration of twisted bilayer graphene (TBG). The moiré pattern resulting from small twist angles significantly modifies the electronic structure, leading to the formation of flat bands at the magic angle. Taken from Ref. [2].

2.1.1 Twisted Bilayer Graphene

Twisted bilayer graphene (TBG) arises when two monolayers of graphene are stacked with a relative twist angle, introducing a purely geometrical long-range interference pattern known as a Moiré superlattice [2]. This structure significantly modifies the electronic properties of the bilayer system compared to the untwisted configurations. The periodicity of the Moiré pattern leads to the formation of new electronic bands, often referred to as mini-bands, which can be dramatically narrower than the original graphene Dirac bands [19].

A key theoretical framework used to understand TBG is the continuum model, developed by Bistritzer and MacDonald [19], which treats the interlayer coupling in the presence of a small twist angle as a perturbation. In this model, the electrons in the two layers hybridize via interlayer tunneling, leading to a reconstruction of the Dirac cones and the emergence of flat bands at specific “magic” angles [2]. These flat bands are characterized by an extremely low Fermi velocity and a high density of states near the charge neutrality point.

The most celebrated of these angles is approximately 1.1° , known as the *magic angle*, where the bandwidth of the lowest-energy bands nearly vanishes. This flattening of the bands amplifies the effects of electron-electron interactions, leading to a rich array of correlated phenomena [2]. At and near this angle, experimentalists have observed unconventional superconductivity [4], Mott-like insulating states, and ferromagnetic behavior, which are absent in monolayer graphene or non-magic-angle bilayers.

From a theoretical perspective, these emergent properties stem from the interplay

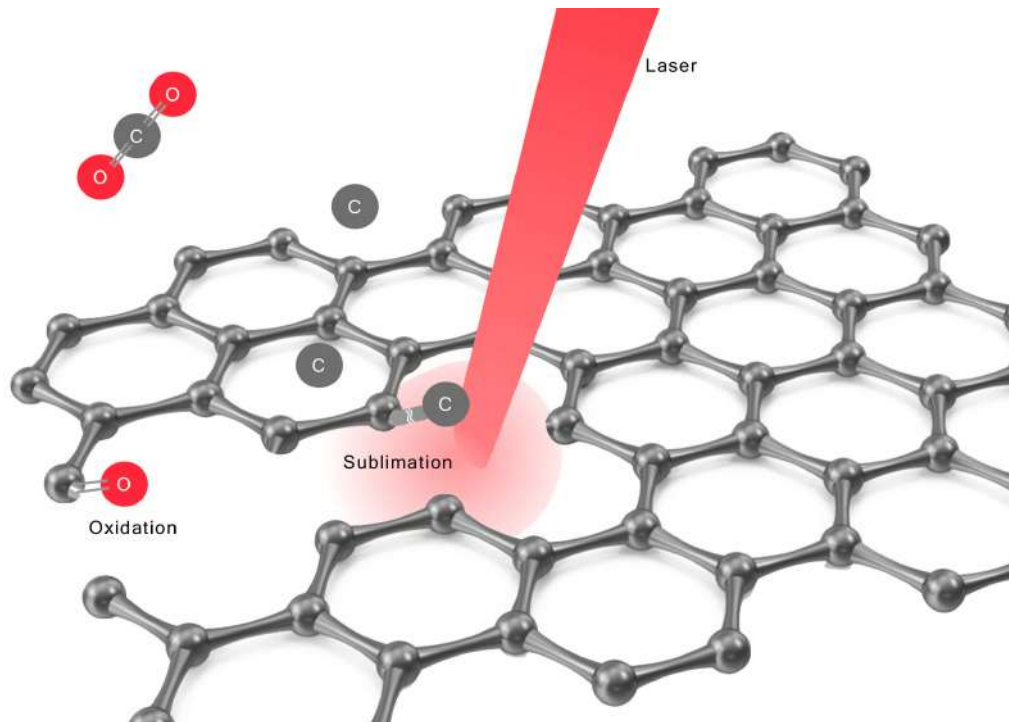


Figure 2.7: Schematic depiction of laser ablation in graphene. The laser locally sublimates carbon atoms, creating precise cuts along defined paths through controlled irradiation. At lower thresholds and below-sublimation-temperature oxidation defect formation occurs.

of strong correlations and topology in the flat bands. The suppression of kinetic energy enhances the relative strength of Coulomb interactions, making the system a fertile ground for exploring strongly correlated phases [4].

The field of magic-angle TBG has rapidly evolved into a broader area often referred to as twistrionics, which explores how electronic behavior can be tuned through interlayer twist.

2.1.2 Graphene Laser Ablation

Graphene ablation refers to the process of removing or structurally modifying graphene using focused laser energy. When laser light interacts with graphene, it can directly break carbon-carbon bonds or induce localized heating, leading to material ejection or modification [20]. The ablation mechanism depends strongly on laser parameters such as wavelength, pulse duration, and energy fluence. Since graphene's absorption of laser energy varies with wavelength, its ablation efficiency also varies accordingly.

In the visible and near-infrared (NIR) regimes, graphene absorbs approximately 2.3% of incident light per layer. This absorption arises primarily from interband transitions, whereby electrons are excited from the valence band to the conduction band upon photon absorption [21]. Because the density of states near the Dirac point is linear and continuous, graphene can absorb a wide range of photon energies without requiring a specific bandgap.

Due to graphene's high thermal conductivity [22], high pulse energy, and low pulse

width are essential (as will be discussed later). Ultrafast lasers (with femtosecond or picosecond pulses) are particularly effective for ablation, as they confine energy deposition both spatially and temporally, minimizing thermal diffusion and collateral damage to surrounding regions [23]. In contrast, nanosecond lasers require higher fluences to induce damage [9, 24].

Ablation can proceed via photothermal effects (heating), photochemical bond breaking, or a combination of both mechanisms [20]. In some cases, non-ablative effects such as defect generation or oxidation may dominate before full ablation occurs. The threshold fluence for ablation varies with substrate and environment. In ambient air, this threshold typically lies around 0.1–0.2 J/cm² [23], and is generally higher under inert conditions [25].

Repeated laser pulses at sub-threshold fluence can cumulatively lead to ablation via the so-called incubation effect, thereby reducing the required energy per pulse [26, 23]. In this case, the reduction in ablation threshold fluence follows a power law:

$$F_{\text{th}} = F_0 \cdot N^{s-1}, \quad (2.19)$$

where N is the number of pulses and $s \approx 0.88$, according to experimental studies [8].

The substrate also influences the ablation threshold—suspended graphene exhibits lower thresholds than substrate-supported graphene due to reduced heat dissipation [20]. High-resolution patterning is achievable with laser ablation, allowing for the fabrication of micro- and nanoscale devices. Additionally, the presence of water or other adsorbates between graphene and the substrate can significantly alter the ablation dynamics, in some cases enhancing or localizing the effect.

Graphene Thermal Conductivity

To analyze the thermal effects occurring during ablation, it is essential to examine the thermal conductivity characteristics of graphene.

Graphene exhibits exceptionally high in-plane thermal conductivity, with values ranging from $K \approx 3080$ to 5150 W/m·K at room temperature for suspended single-layer graphene (SLG) [27]. This high conductivity is primarily due to the efficient transport of phonons—especially out-of-plane flexural acoustic (ZA) phonons—which dominate thermal transport because of a selection rule that suppresses their anharmonic scattering in SLG [28].

The ZA phonon branch in graphene follows a quadratic dispersion relation, $\omega_{\text{ZA}} \propto q^2$, unlike the linear dispersion of longitudinal acoustic (LA) and transverse acoustic (TA) phonons. While this leads to a vanishing group velocity $v_g = \partial\omega/\partial q$ near $q \rightarrow 0$, the high density of states and long phonon lifetimes compensate, contributing significantly to overall thermal conductivity.

The lattice thermal conductivity can be modeled via the Boltzmann Transport Equation (BTE), where it is expressed as:

$$\kappa_L = \sum_{\lambda} \int \frac{\hbar^2 \omega_{\lambda}^2}{k_B T^2} \tau_{\lambda} v_{\lambda}^2 n_0 (n_0 + 1) D(\omega_{\lambda}) d\omega, \quad (2.20)$$

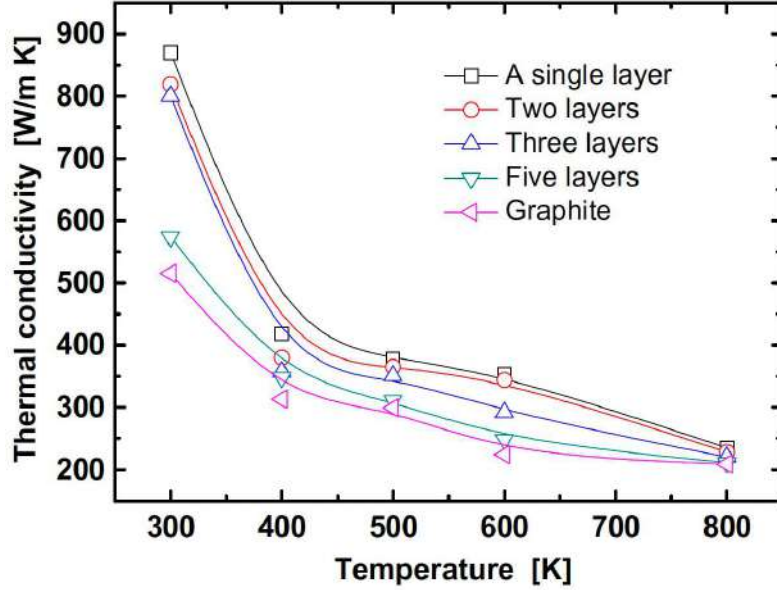


Figure 2.8: Thermal conductivity of suspended graphene as a function of temperature and layer number. The conductivity decreases with increasing layer number due to enhanced phonon scattering. Taken from Ref. [22].

where τ_λ is the phonon relaxation time, v_λ is the group velocity, n_0 is the Bose-Einstein distribution, and $D(\omega)$ is the phonon density of states.

Flexural phonons contribute strongly to thermal conductivity because three-phonon scattering processes are suppressed by reflection symmetry in single-layer graphene. However, in multilayer graphene (MLG) or graphite, weak van der Waals interlayer coupling breaks this symmetry, lifting the selection rule and enabling additional scattering channels such as $\text{ZA}+\text{ZA} \leftrightarrow \text{ZA}$ and $\text{ZA}+\text{TA} \leftrightarrow \text{LA}$ [28]. This results in a significant reduction in thermal conductivity.

Numerical simulations and experiments show that κ_L decreases rapidly with increasing layer number N , approaching the graphite limit of approximately 2000 W/m·K by $N = 5$ [22].

This layer-dependent reduction in thermal conductivity is consistent with the observed behavior during laser ablation of MLG [9], where less energy is required to ablate multilayer graphene than monolayer graphene. The effect is attributed to a dimensional crossover in specific heat capacity, primarily governed by the flexural phonons discussed above (c_f). As the number of layers increases, the specific heat decreases. Another contribution to the specific heat, denoted c_a , becomes relevant as the material transitions toward bulk behavior. The energy threshold (per unit mass) for nanosecond UV laser ablation has been modeled as:

$$E_{\text{th}} \text{ (J/cm}^2\text{)} = C_0 N^{-0.38} (c_f + c_a) = C_0 N^{-0.38} [N^{-1} + (1 - e^{-N/N_0})], \quad (2.21)$$

where $C_0 = 0.8$ and $N_0 = 7.4$. Furthermore, the absorption of multilayer graphene in the UV regime has been reported to scale as $\alpha \propto N^{0.38}$ [9].

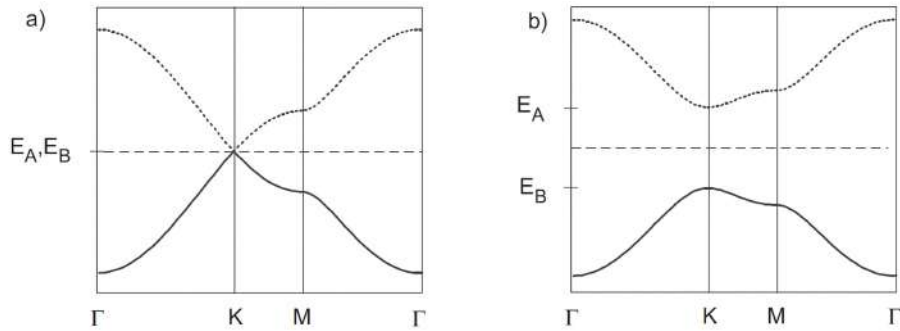


Figure 2.9: Electronic band structure comparison between graphene (a) and hexagonal boron nitride (hBN) (b). hBN exhibits a wide bandgap, making it an ideal insulating and encapsulating material for graphene. Taken from Ref. [29].

2.1.3 hBN-encapsulated Graphene

Hexagonal boron nitride (hBN) is a two-dimensional material composed of boron and nitrogen atoms arranged in a honeycomb lattice, structurally similar to graphene. The band structure of hBN can be determined with the tight-binding model as done with graphene, the only main difference is that the self energies are no longer 0 but have a value due to the symmetry-break at the Bor and Nitrogen lattice sites. This results in energy eigenvalues

$$E_{\text{hBN}}(\vec{k}) = \pm \sqrt{M_0^2 + \gamma_0^2 \left(1 + 4 \cos^2 \left(\frac{k_y a_0}{2} \right) + 4 \cos \left(\frac{\sqrt{3} k_x a_0}{2} \right) \cos \left(\frac{k_y a_0}{2} \right) \right)}. \quad (2.22)$$

where $M_0 = \frac{E_B - E_N}{2}$, where E_N and E_B are the onsite energies of the N and B atoms, respectively [15].

This results, as shown in Fig. 2.9, in a wide band gap of approximately 5.9 eV and makes hBN act as an excellent electrical insulator while maintaining high thermal conductivity.

Its atomically smooth surface and lack of dangling bonds make it an ideal substrate for two-dimensional electronics. In van der Waals heterostructures, hBN is commonly used as a dielectric layer or encapsulating material, significantly improving device performance [30] [31].

Encapsulating graphene with hexagonal boron nitride (hBN) has become a standard technique to enhance the electronic quality of graphene-based devices. Graphene placed directly on silicon dioxide suffers from surface roughness, charge traps, and impurities that degrade mobility [32]. hBN provides an atomically flat, chemically inert, and lattice-matched interface, minimizing these issues. When encapsulated between two hBN layers, graphene exhibits ultra-high carrier mobility and reduced charge inhomogeneity. This technique allows for the observation of ballistic transport over micrometer distances and the quantum Hall effect at low magnetic fields [33].

Experiments by *Dean et al. (2010)* [33] demonstrated that hBN substrates pre-

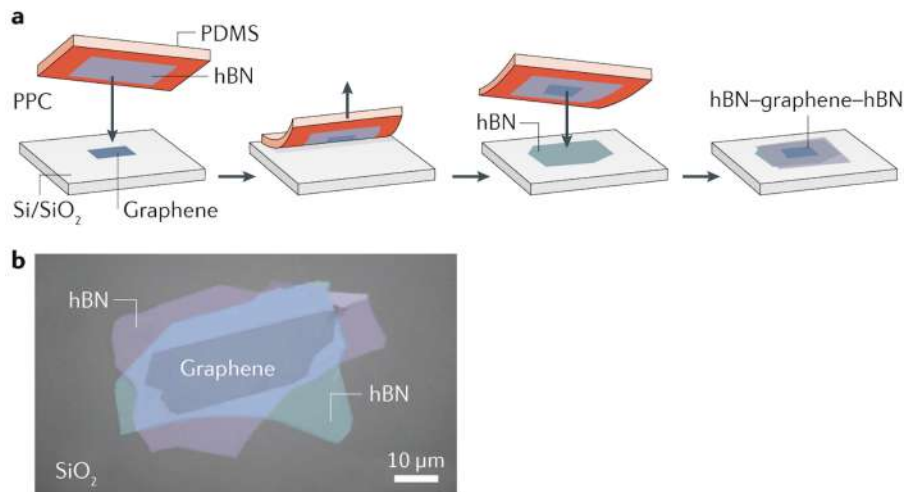


Figure 2.10: (a) Illustration of the dry transfer technique used to encapsulate graphene between hexagonal boron nitride (hBN) layers. A polymer stamp composed of polydimethylsiloxane (PDMS) and a polypropylene carbonate (PPC) film with an hBN flake is used to pick up a graphene flake exfoliated on a SiO₂/Si substrate. The hBN-graphene stack is then aligned and placed onto another hBN flake to complete the heterostructure, forming a sandwiched hBN-graphene-hBN stack. (b) Optical micrograph of the resulting heterostructure on a SiO₂ substrate, showing the graphene flake encapsulated between two hBN flakes. Adapted from [30].

serve the intrinsic properties of graphene far better than a SiO₂. Encapsulation also suppresses environmental doping and protects the graphene from adsorbates and moisture. The process typically involves mechanical exfoliation of hBN and graphene flakes, followed by a dry-transfer stacking method using a polymer stamp under a microscope. The hBN-graphene-hBN stack is then placed on a substrate, and electrical contacts are made by etching through the hBN layers. This approach reduces interfacial disorder and eliminates contamination from wet chemistry. Devices fabricated this way show sharp Dirac points and minimal hysteresis in gate response.

Especially interesting for the experiments pursued in this thesis is the absorption of hBN, specifically in the NIR regime. The photon energy at 1064 nm is of

$$E_{ph} = \frac{hc}{\lambda} \sim 1.17eV \quad (2.23)$$

which lies well below the band gap of hBN and makes it transparent to 1064 nm light in the absence of defects and impurities.

2.2 Optics

A significant part of this thesis involved the construction of an optical setup primarily composed of a microscope and a laser. Various optical components had to be installed to achieve the desired functionalities. This section outlines the main concepts and working principles of these components.

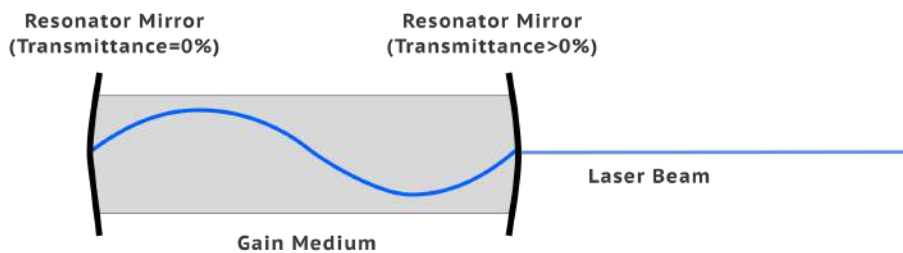


Figure 2.11: Schematic diagram of laser operation based on stimulated emission and optical amplification inside a resonator cavity. Replicated from Ref. [20].

2.2.1 Laser

Laser stands for **Light Amplification by Stimulated Emission of Radiation**. It operates by using an external pump source to excite electrons in a material known as the gain medium (Fig. 2.11), raising them from a lower energy level E_1 to a higher energy level E_2 . This energy input creates a *population inversion*, meaning more electrons occupy the excited state E_2 than the ground state E_1 —a necessary condition for laser action. [34]

When one of these excited electrons returns to the lower energy level, it may emit a photon. If this de-excitation is triggered by an incoming photon of the same energy, the process results in *stimulated emission*, producing a new photon that is coherent (same phase, direction, and energy) with the original. These photons are reflected back and forth within an optical resonator—typically composed of two mirrors—leading to repeated amplification of light as it passes through the gain medium. One of the mirrors is partially transparent, allowing a portion of the coherent light to exit the cavity as a narrow, intense laser beam. [35]

It is important to note that a two-level system cannot sustain a population inversion [36]. This is because the same photons used to excite electrons from the lower to the upper level can also stimulate emission, preventing the upper level from becoming more populated. As a result, the rates of excitation and de-excitation balance each other, making laser action impossible in such a configuration. Therefore, practical lasers require at least three or four energy levels to decouple the pumping process from the lasing transition and enable a stable population inversion.

Lasers can be classified according to their mode of operation as either *continuous wave* (CW) or *pulsed* lasers [37]. A CW laser emits a constant, uninterrupted beam of light as long as the pump source supplies energy, resulting in a steady output power. In contrast, a pulsed laser emits light in short, discrete bursts, with pulse durations ranging from femtoseconds to nanoseconds, separated by intervals of no emission.

Pulsed operation is achieved using techniques such as Q-switching or mode-locking, which modulate either the gain or the phase conditions within the laser cavity to store and periodically release energy [37]. As a result, pulsed lasers can achieve very high *peak powers* during each pulse, even if their average power remains relatively low. This makes pulsed lasers particularly useful in applications requiring precise energy delivery with minimal thermal effects. [38]

The core parameters that characterize such lasers—apart from the wavelength—are

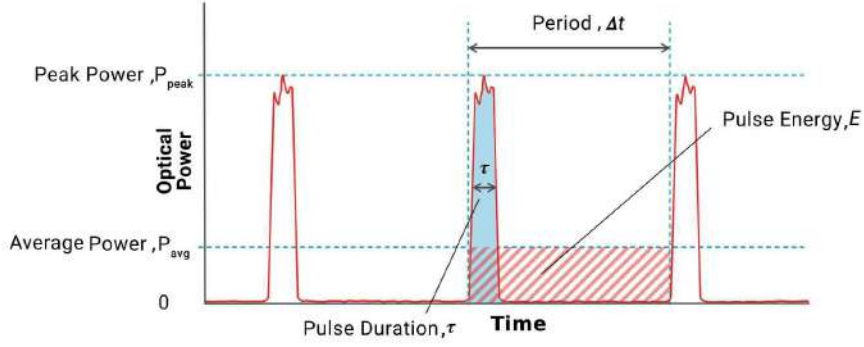


Figure 2.12: Illustration of pulsed laser emission showing pulse duration, repetition rate, and energy distribution over time. Taken from Ref. [39].

[40]:

- **Pulse duration** τ : Defines the time over which the energy of a single pulse is distributed.
- **Repetition rate** f : Indicates how many pulses are emitted per second.
- **Average power** P_{avg} : The total energy output per second, i.e., the sum of all pulse energies normalized over one second.

From these parameters, two important derived quantities can be calculated [41]:

- **Pulse energy** E_{pulse} : The energy contained in a single laser pulse, given by:

$$E_{pulse} = \frac{P_{avg}}{f} \quad (2.24)$$

- **Peak power** P_{peak} : The maximum instantaneous power during a pulse, calculated as:

$$P_{peak} = \frac{E_{pulse}}{\tau} \quad (2.25)$$

2.2.2 Microscope

A huge part of the thesis was the building of a microscope. A microscope is an optical instrument that creates an enlarged image of an object and allows a detailed observation [42]. It typically consists of an objective and an eyepiece. In the case of infinity-corrected microscopes, the objective lenses produce parallel light rays, which are then focused by a separate tube lens before the eyepiece (Fig. 2.13) [43]. In case of digital microscopy there is no need of an eyepiece lens. This design allows the insertion of filters or other optical components between the objective and tube lenses without distorting the image [44]. The resulting magnification is:

$$v = \frac{f_{tube}}{f_{obj}} \quad (2.26)$$

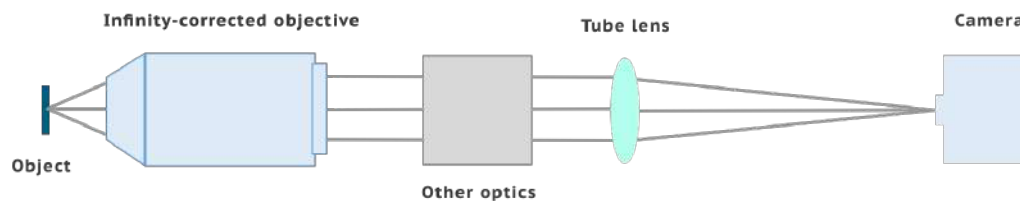


Figure 2.13: Schematic optical path of an infinity-corrected microscope, showing how parallel rays are focused through the tube lens before image acquisition.

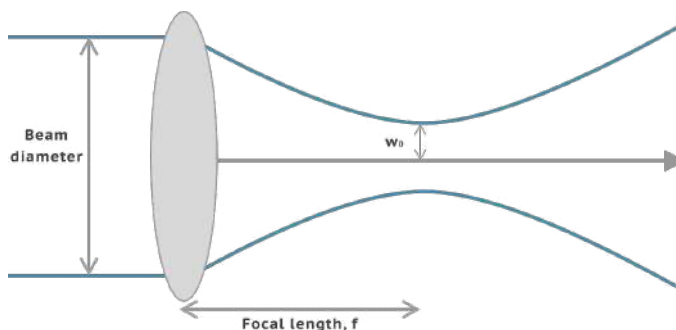


Figure 2.14: Illustration of the diffraction-limited laser spot size as determined by beam waist, wavelength, and numerical aperture.

2.2.3 Diffraction Limit

The diffraction limit in a microscope refers to the fundamental limit on the spatial resolution imposed by the wave nature of light. The fundamental definition was first formulated by Ernst Abbe in 1873 and states that the minimum resolvable distance between two points is limited by [45]:

$$d = \frac{\lambda}{2NA}, \quad (2.27)$$

where λ the wavelength of light is and NA the numerical aperture.

Some years later in 1896, Lord Rayleigh formulated a rather more conservative limit than Abbe's and claimed that two point sources were considered resolvable only when the principal maximum of one's Airy disk coincides with the first minimum of the other. This translates into the following criterion [45]:

$$d = \frac{1.22\lambda}{2NA}, \quad (2.28)$$

In this context the minimal size of a focused laser beam, also known as beam waist, can be determined. For a laser beam with a Gaussian profile, the minimal spot size at the focus is given by [46]:

$$d = 2w_0 = \frac{2\lambda}{\pi NA}, \quad (2.29)$$

where w_0 is the beam waist, which means the radius at which intensity falls to $1/e^2$ of maximum.

2.2.4 Dichroic mirror

A dichroic mirror is an optical component designed to reflect certain wavelengths of light while transmitting others. In the case of shortpass dichroic mirrors, wavelengths below a defined cutoff are transmitted, while wavelengths above the cutoff are reflected. [47]

The working principle of dichroic mirrors relies on the phenomenon of thin-film interference. When light encounters a thin film, part of it is reflected from the film's top surface, while another portion penetrates the film and reflects off the lower interface. These two reflected waves can then interfere with each other. Depending on the optical path difference—which depends on the film's thickness, the wavelength of the incident light, and the angle of incidence—this interference can be constructive or destructive. Constructive interference enhances reflection, whereas destructive interference allows transmission. [48]

In dichroic mirrors, multiple thin layers of dielectric materials with varying refractive indices are deposited in sequence. By carefully designing the thickness and refractive index contrast of these layers, specific interference effects can be engineered. As a result, dichroic mirrors can be tailored to reflect a defined spectral range while transmitting the complementary range. [48]

2.2.5 Beam Collimator

A beam collimator is an optical device that transforms divergent light rays—such as those emitted from an optical fiber—into a collimated beam, i.e., a beam composed of parallel rays. [49]

This is achieved by placing one or more lenses at specific distances from the light source to manipulate the beam's divergence. The key factors in designing or selecting a suitable beam collimator include the type of optical fiber connector, the numerical aperture (NA) of the fiber, and the desired waist diameter of the output beam. [49]

First, the collimator's input must be compatible with the fiber's connector type (e.g., FC/PC, FC/APC) to minimize insertion losses. Second, the numerical aperture of the collimator should be greater than or equal to that of the fiber to ensure efficient light collection and transmission. [50]

Finally, the waist diameter of the resulting beam must be considered. This is defined as the beam's theoretical $1/e^2$ diameter at one focal length from the lens and depends on both the focal length f and the numerical aperture of the collimator [51]:

$$D \approx 2f \cdot \text{NA}. \quad (2.30)$$

2.3 Optical Contrast

Optical contrast is a non-destructive method used to determine the number of graphene layers on a SiO_2/Si substrate [52]. When white light is incident on such a sample, part of the light is reflected directly from the top surface of the graphene,

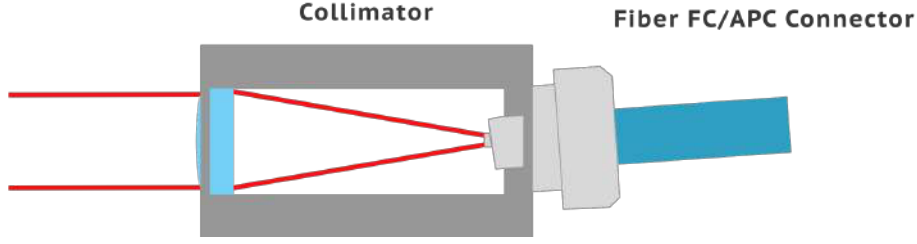


Figure 2.15: Schematic structure of a fiber collimator, which converts divergent light from an optical fiber into a collimated laser beam.

while another part passes through the graphene and is reflected back from the SiO_2/Si interface. These two reflected beams interfere—constructively or destructively—depending on the optical path difference, which alters both the intensity and color of the reflected light [53].

Graphene layers influence this interference by absorbing light and modifying the phase of the reflected beam. As a result, the reflectivity of the system changes in a layer-dependent manner, allowing estimation of layer thickness through optical imaging [53] [52].

The intensity of the reflected light can be expressed as:

$$\begin{aligned}
 I(n_1) = & \left| \left(\frac{n_0 - n_1}{n_0 + n_1} e^{i(\Phi_1 + \Phi_2)} + \frac{n_1 - n_2}{n_1 + n_2} e^{-i(\Phi_1 - \Phi_2)} + \frac{n_2 - n_3}{n_2 + n_3} e^{-i(\Phi_1 + \Phi_2)} \right) \right. \\
 & \times \left(e^{i(\Phi_1 + \Phi_2)} + \frac{n_0 - n_1}{n_0 + n_1} \frac{n_1 - n_2}{n_1 + n_2} e^{-i(\Phi_1 - \Phi_2)} \right. \\
 & \left. \left. + \frac{n_0 - n_1}{n_0 + n_1} \frac{n_2 - n_3}{n_2 + n_3} e^{-i(\Phi_1 + \Phi_2)} + \frac{n_1 - n_2}{n_1 + n_2} \frac{n_2 - n_3}{n_2 + n_3} e^{i(\Phi_1 + \Phi_2)} \right)^{-1} \right|^2
 \end{aligned} \quad (2.31)$$

where: - n_0 is the refractive index of air (assumed to be 1), - n_1 is the refractive index of graphene, - n_2 is the refractive index of SiO_2 , - n_3 is the refractive index of silicon (Si) [52].

The phase shifts are given by:

$$\Phi_1 = \frac{2\pi n_1 d_1}{\lambda}, \quad \Phi_2 = \frac{2\pi n_2 d_2}{\lambda},$$

where d_1 is the thickness of the graphene, d_2 is the thickness of the SiO_2 layer, and λ is the wavelength of the incident light. All refractive indices are wavelength-dependent.

The contrast C introduced by a graphene monolayer is defined as:

$$C = \frac{I(n_1 = 1) - I(n_1(\lambda))}{I(n_1 = 1)}. \quad (2.32)$$

It was found that when the SiO_2 layer is approximately 280 nm thick, the optical contrast is maximized in the green region of the visible spectrum [53]. This makes it easier to identify graphene flakes under an optical microscope.

Furthermore, the contrast increases almost linearly with the number of graphene layers up to about nine layers [7]. This relationship enables the determination of

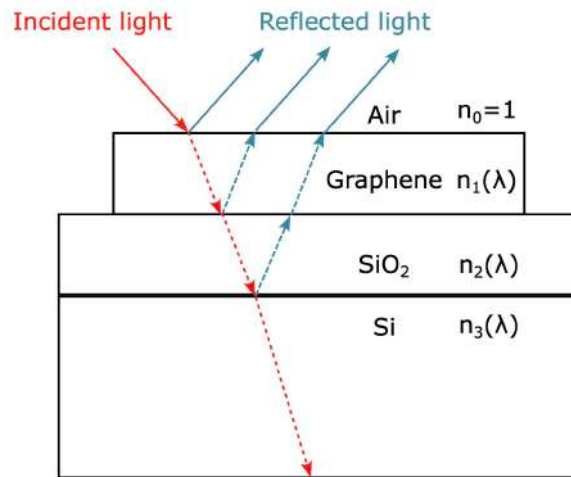


Figure 2.16: Optical interference model for a monolayer graphene flake on a 280 nm SiO₂/Si substrate substrate. Multiple reflections at interfaces create interference patterns used for layer identification. Adapted from Ref. [53].

graphene thickness by analyzing the variation in green channel intensity between the bare substrate and the flake.

Chapter 3

Methods

Building on the theoretical foundation presented in the previous chapter, this section details the experimental setup and procedures developed to investigate laser ablation of graphene. Particular attention is given to the construction of a custom laser-cutting microscope, the development of a software interface for precise sample manipulation and laser control, and the calibration techniques employed to ensure accuracy. These methods enabled studies of ablation thresholds across different graphene layer counts and exposure times.

3.1 Laser-Cutting Microscope

The core of this thesis involved constructing a microscope capable of cutting graphene — even multilayer graphene — while reusing as many existing components as possible, which the research group with which this bachelor thesis was made had. A microscope unit with its camera and a motion-controller device could be repurposed for this aim. However, the use of older equipment came with drawbacks.

3.1.1 Building the Microscope

The first step toward achieving a graphene-cutting-capable microscope is to understand the conditions necessary to cut graphene. As discussed in different papers, the fluence required to reach the ablation threshold lies between 130 mJ/cm^2 and 270 mJ/cm^2 [26] [54], depending on the laser characteristics. This refers to single-pulse ablation, i.e., the energy density needed in a single laser pulse to break carbon bonds and sublimate. Later, we will also address the incubation effect — how prolonged irradiation over several milliseconds lowers the effective threshold [23].

The research group already had access to a high-power pulsed near-infrared (NIR) laser. The NPI Laser [55] operates at a wavelength of 1064 nm , a frequency of 50 MHz , a pulse width of 15 ps , and an average power of 200 mW . With these specifications, several considerations arise. For these specifications, the threshold lies at about 200 mJ/cm^2 [26] [23].

First, the energy per pulse is defined by Eq. (2.24). For our laser, this is $E_{\text{pulse}} = 4 \text{ nJ}$. Based on this value, we can calculate the maximum laser spot size required to achieve

the ablation threshold. This means how small (i.e., maximum diameter) the laser light must be focused in order to achieve the necessary energy per surface. Assuming it is a Gauss beam, the maximum diameter is given by:

$$d_{\max} = \sqrt{\frac{4E_{\text{pulse}}}{\pi F_{\text{TH}}}} = 1.6 \mu\text{m},$$

where $F_{\text{TH}} = 200 \text{ mJ/cm}^2$ is the threshold fluence.

From optics, it is known that the smallest achievable spot size for a collimated beam (with wavelength λ) and an objective lens (with numerical aperture NA) is given by Eq. (2.29): $d = \frac{2\lambda}{\pi \text{NA}}$. Assuming $d_{\min} = 1.4 \mu\text{m}$ and $\lambda = 1064 \text{ nm}$, the minimum numerical aperture can be estimated:

$$\text{NA}_{\min} = \frac{2 \cdot 1064 \text{ nm}}{\pi \cdot 1400 \text{ nm}} = 0.48$$

Smaller spot sizes (i.e., higher NA) result in cleaner and narrower cuts.

The Olympus LC Plan N 50x/0.65 IR [56] objective is well-suited for this purpose, offering a high NA and being optimized for NIR light. However, it exhibits reduced transmission in the visible spectrum, which affects camera imaging. To address this, users can switch objectives for optimal visualization.

The final setup of the microscope is shown in Figure 3.2, and Figure 3.1 illustrates the components and structure. The microscope unit used is the Mitutoyo VMU-V [57], equipped with a tube lens with a focal length of 200 mm, which connects the camera and the white light source to the probe. Below the white-light component, a custom aluminum adapter mounts a Thorlabs cage system [58] that integrates the laser into the optical path. Beneath the cage system, another custom aluminum piece connects the objective turret.

As the light after the main microscope unit is collimated (infinity-corrected microscope) [43], the path can be expanded arbitrarily, which allows the usage of the cage system to append the laser beam to the optics. The key component, placed inside the cage system and deflecting the laser into the objective, is a short-pass dichroic mirror [59] (with cutoff length at 850 nm), which transmits wavelengths below 850 nm and reflects longer wavelengths. This minimizes optical losses and protects the camera from potential damage caused by laser exposure. The laser beam exits the optical fiber through a collimator [60], which expands the beam to approximately 4 mm and enables almost full use of the objective's NA.

It must be taken into consideration that along the optical path — due to the beam collimator, mirror, dichroic mirror, and the objective itself — a certain percentage of the laser light is lost. Therefore, the numerical aperture (NA) of the objective must be sufficiently high to ensure that the resulting fluence at the sample plane exceeds the ablation threshold.

With the current set of components and microscope, the measured average power after the objective is:

$$P_{\text{avg}} = (155.4 \pm 0.5) \text{ mW}$$

This means that the transmittance of the whole optical system is about 77%, which is typical in microscope systems.

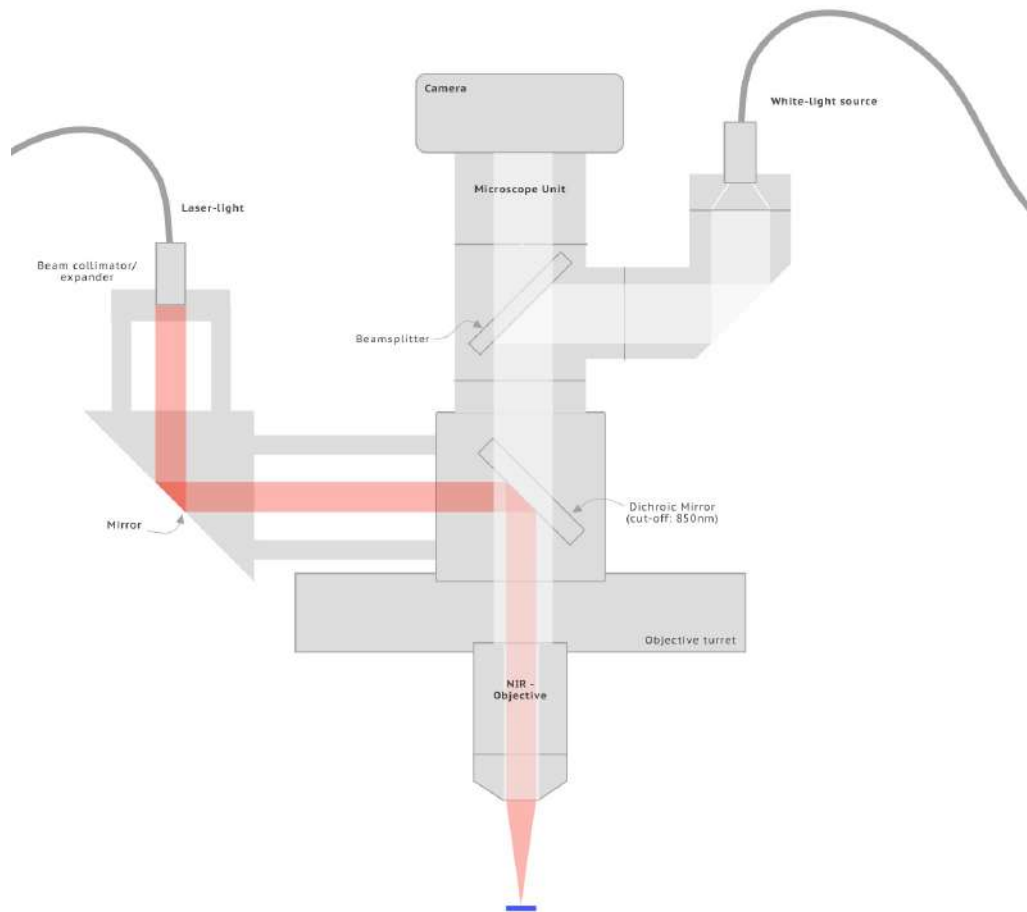


Figure 3.1: Schematic structure of the constructed laser-cutting microscope, integrating the camera, optics, dichroic mirror, and laser coupling for precise graphene ablation.

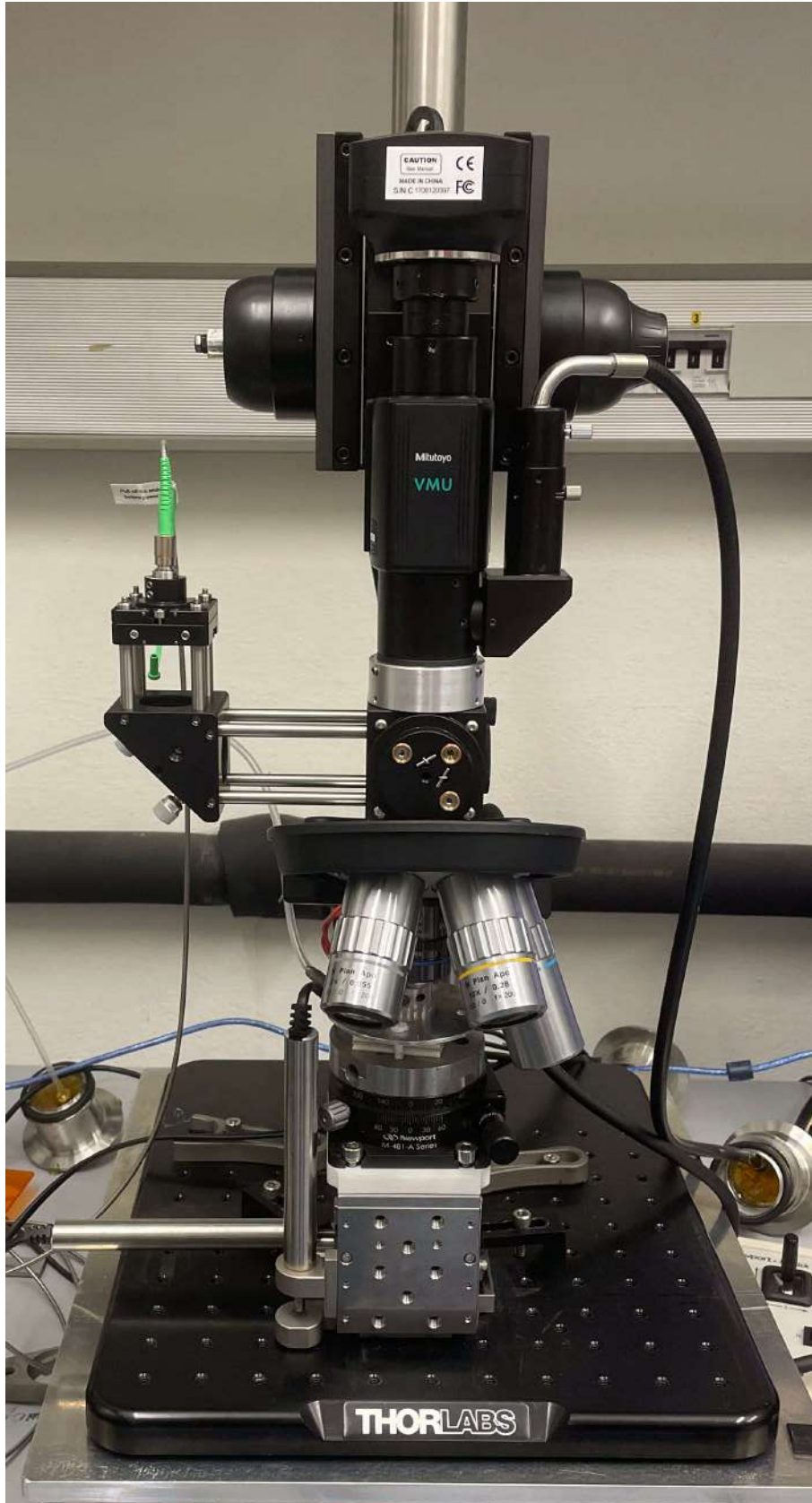


Figure 3.2: Photograph of the final laser-cutting microscope setup showing all key components assembled, including the microscope unit, cage system, and motorized sample stage.

This corresponds to a pulse energy of

$$E_{\text{pulse}} = (3.11 \pm 0.01) \text{ nJ}$$

and, assuming an approximate spot diameter of

$$d_{\text{spot}} = (1.3 \pm 0.2) \mu\text{m},$$

yields a resulting fluence defined as $F = \frac{E_{\text{pulse}}}{A} = \frac{E_{\text{pulse}}}{\pi(d_{\text{spot}}/2)^2}$ of:

$$F_{\text{pulse}} = (234 \pm 72) \text{ mJ/cm}^2$$

In conclusion, this calculation confirms that a single laser pulse under the given configuration should already be sufficient to ablate or cut a graphene flake.

Incubation effects due to prolonged irradiation should, as discussed previously, lower the threshold. [23]

An essential aspect of the construction is sample movement, allowing an autonomous cutting process. This is achieved with three ESP301 stepper motors [61], one per axis, controlled via a Newport motion controller. These motors allow sub-micron precision but suffer from significant backlash errors ($\sim 1 \mu\text{m}$), which is large for our application since the samples are on the scale of $\sim 10 - 20 \mu\text{m}$. To mitigate this, a software-based error correction was implemented, which will be described in the next section.

On the other hand, safety must be addressed. This laser is extremely powerful and is capable of significantly damaging the retina. The fact that the user does not see the laser spot (IR-laser) makes it even more important to take appropriate safety measures. Concerning the construction (as shown in Fig. 3.1), it was designed to avoid any possible interaction in the laser's optical path. Nonetheless, the use of safety glasses is mandatory when interacting with the laser.

3.1.2 Building the Graphical User Interface (GUI)

To ensure smooth operation of the microscope and enable autonomous, reliable, user-friendly cutting, a complete Graphical User Interface (GUI) (Fig. 3.3) was developed using Python, specifically the PyQt5 library. This software enables simultaneous control of the camera (for visualization), the stepper motors (for positioning), and the laser (for cutting). The code is organized across multiple Python files, which are discussed in detail in the Appendix A.

To retrieve camera data, the open-source library `amcam.py` was used [62]. This API handles data from an AmScope camera connected via USB and displays the image as a QPixmap in a Python `QLabel` widget. The left side of the GUI displays the live camera image, allowing the user to interact with the cut designs directly on it.

On the right side, the user can control both the motors (i.e., the sample position) and the laser. Communication with the motor controller and the laser controller occurs via serial communication in ASCII format. The software translates user inputs from the GUI into ASCII commands, which are then sent to the respective controllers.

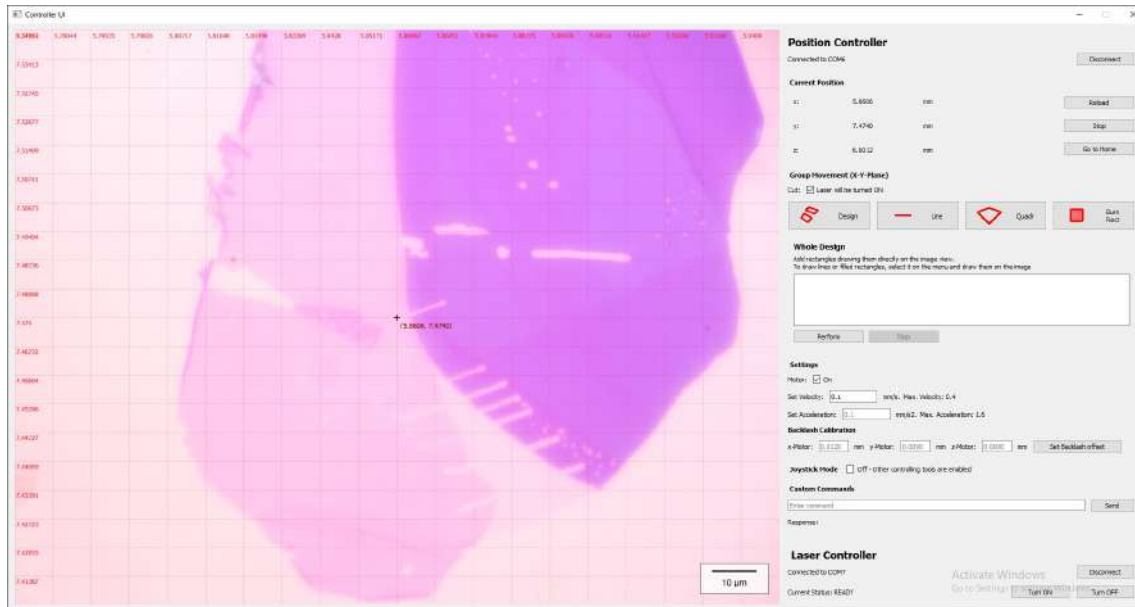


Figure 3.3: Graphical User Interface (GUI) developed for microscope control. The interface allows real-time sample visualization, laser control, and motion programming for precise cuts.

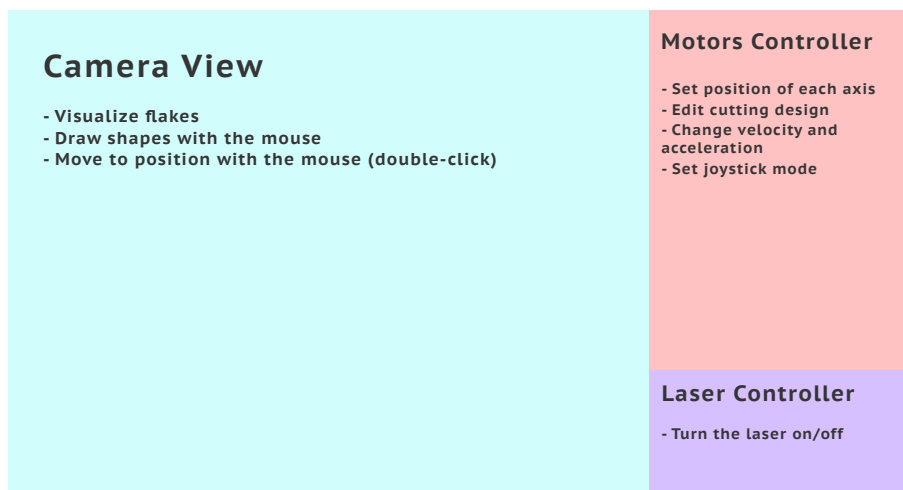


Figure 3.4: Schematic structure of the GUI, highlighting its main functional blocks: camera visualization, motor control, and laser control.

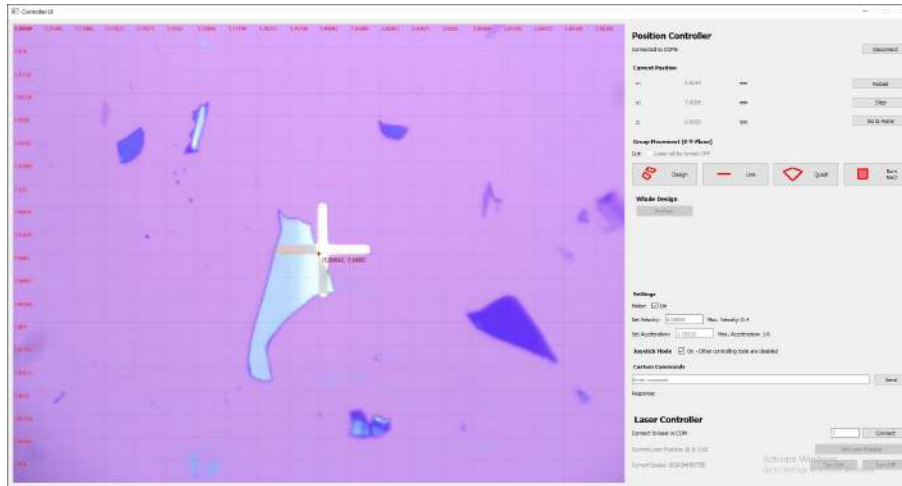


Figure 3.5: Calibration cross used for pixel-to-distance conversion. This reference allows accurate transformation of GUI-drawn shapes into real-world motor coordinates.

In the position controller section, users can move the motors within a range of 0 to 12 mm, the limits of the motors themselves. Both speed and acceleration can be configured, up to 0.4 mm/s and 1.8 mm/s², respectively. A joystick can also be used to control movement by enabling the "Joystick Mode", which simplifies the search for the flake or navigating larger distances. However, this mode must be disabled when drawing or performing a cut.

The core functionality lies in the "Design" section. Here, users can create geometrical elements such as lines, rectangles, or quadrilaterals. The resulting design defines the coordinated motion of the x- and y-axis motors to cut specific shapes into the graphene flake. These shapes facilitate the stacking process described earlier, making it cleaner and more accurate. Shapes can be added either by manually entering coordinates or by using the mouse to draw directly onto the camera view. The elements appear in a list in the "Whole Design" tab. Figure 3.8 shows an example with two adjacent rectangles. All design elements can be added, moved, rotated, and deleted intuitively using mouse and keyboard controls within the image viewer.

Coordinates Transformation Between Pixels and Real World Position

A major challenge was translating mouse positions on the screen into real-world coordinates on the sample. This requires determining how many pixels correspond to one micrometer. To calibrate this, the movement of the motors across various test samples with etched crosses of known dimensions was analyzed. Static tracking and controlled movements yielded the following pixel-to-distance conversion:

$$1 \text{ pixel} = (8.9 \pm 0.3) \cdot 10^{-5} \text{ mm}$$

To support drawing shapes onto the camera image, coordinate grids were drawn on the camera image.

The software tracks (on double-click or click-hold) the pixel position of the mouse relative to the center of the image, which corresponds to the current motor po-

sition. This position relative to the image center is then transformed using the pixel-to-distance conversion (3.1.2) to the real-world position relative to the center (current motor position). When drawing whole shapes, all these pixel coordinates are transformed to real-world coordinates and stored in the Design tab.

The process to determine the conversion number was the following: First, an approximate value for the conversion was guessed. With the converted coordinates drawn into the camera view, a movement to the edge of the cross on the sample was ordered. Depending on whether the arrival destination after the movement surpassed the cross edge or didn't reach it, the conversion was adapted. This process was repeated several times to achieve higher reliability. The error is due to the impossibility of optically determining the exact point.

For the cutting process, there are four different design components available: line, rectangle, quadrilateral, and filled rectangle. The filled rectangle allows for complete ablation of an area rather than just cutting the contour (as the others). This helps in removing unwanted flake material and isolating the desired area. A quadrilateral is essentially a rectangle with independently adjustable corner coordinates. When a rectangle is drawn, a buffer area is automatically added around it. This buffer width is customizable and helps to ensure a clean pickup zone during stacking.

The software sends specific ASCII commands to the motion controller during the cutting process. Additional commands can be sent manually through the custom command input bar.

Beneath the position controller, the laser control panel is located. Like the motors, the laser is controlled via serial ASCII communication. An extended list of important commands for the motion controller and laser controller is provided in the appendix B.

Clicking the "Laser ON" button triggers a warning dialog reminding users of safety procedures. After that, an informational message appears to note the chromatic aberration: the focus point for visible light differs from that for infrared laser light. Therefore, before clicking the "Perform" button to start the cut, the user must adjust the focus for the laser — even if it worsens visual feedback.

The Design and Cutting Process

The full procedure of a typical cut is as follows:

After launching the GUI, the camera activates, and both the laser and motion controller connect via serial communication (COM ports must be selected). The flake is located using either the joystick or manual coordinate input. It is recommended to use a separate microscope with better imaging software to identify suitable flakes and determine their thickness, since the GUI's camera API has limited image quality and capabilities.

Once the flake is centered in the camera view (Figure 3.7) and the joystick mode is turned off, shapes can be drawn using the mouse — such as two adjacent rectangles with a deletion surface around them (Figure 3.8). Before executing the cut, the focus must be changed to optimize laser sharpness. This is done by turning the laser on over an unused area of the sample and adjusting the focus until the laser

Pseudocode Diagram of Cutting-Design

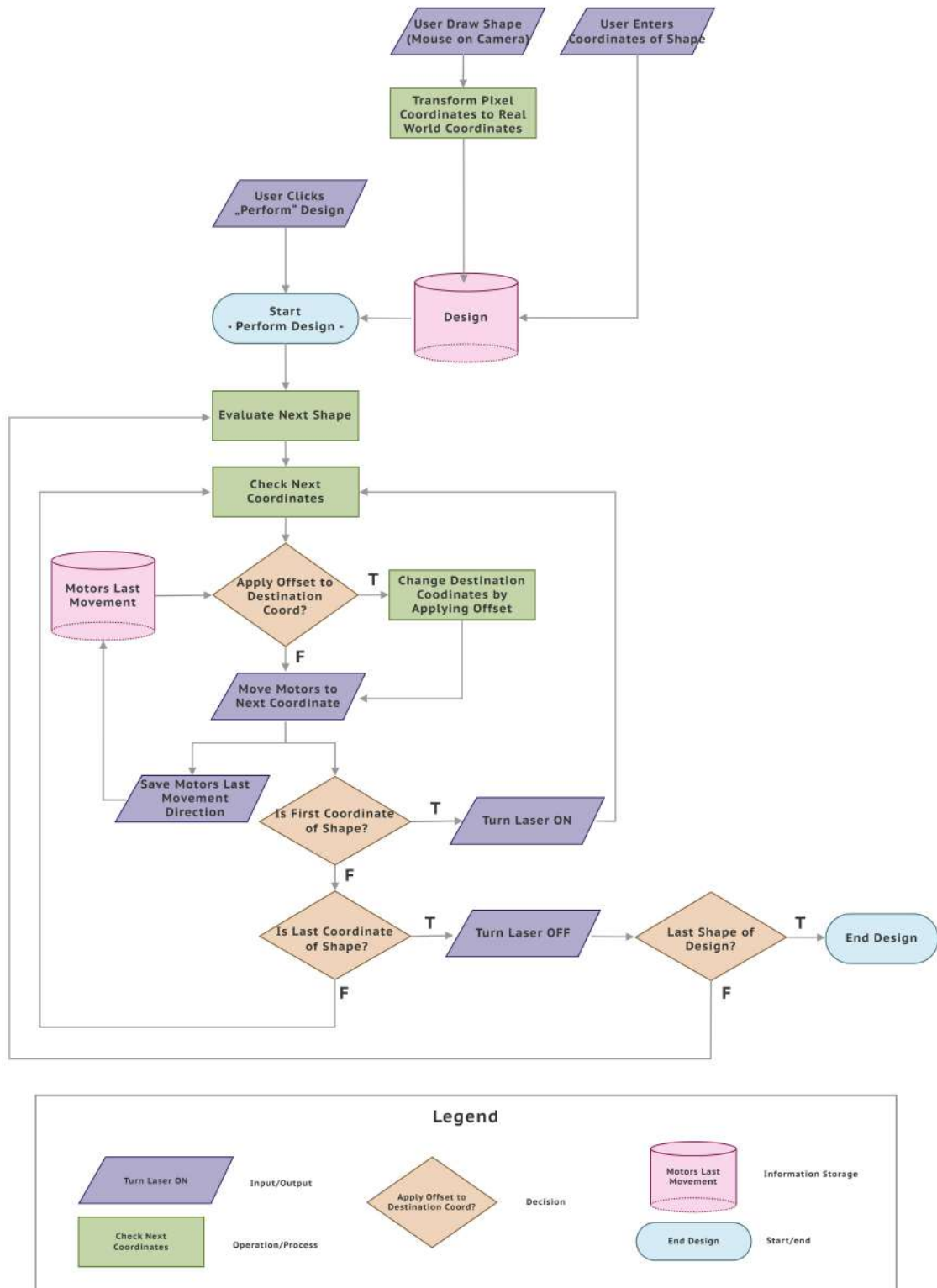


Figure 3.6: Pseudocode flow diagram illustrating the logic and sequence of the cutting procedure, from design to execution and safety measures.

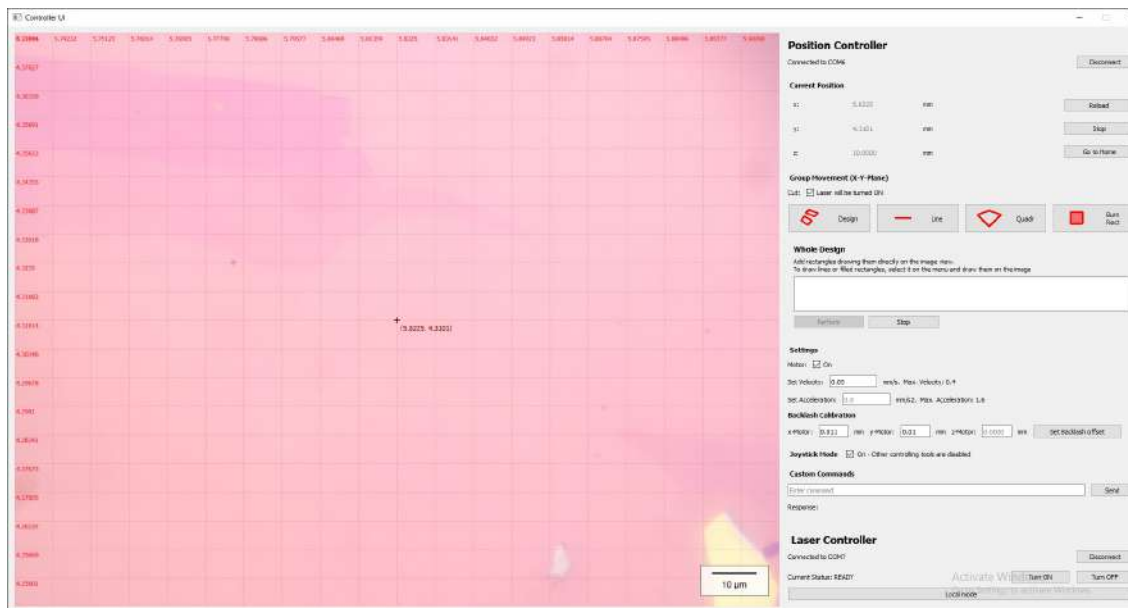


Figure 3.7: Camera image showing a graphene flake before laser cutting. The central alignment allows direct drawing of cutting geometries onto the flake.

spot appears smallest. Even if this method does not guarantee the smallest possible laser spot, it is experimentally sufficient for cutting. Then, the laser is turned off again. Without changing the focus and after taking appropriate safety measures, the user clicks “Perform.” Once the motion sequence completes, the laser is automatically deactivated and the focus can be readjusted for improved visualization. An example result is shown in Figure 3.9.

Before cutting, make sure that optimal speed and acceleration values are configured. Based on experimental evaluation, the following parameters yield good results in terms of cut quality and processing time:

$$v_{\text{opt}} = 0.05 \text{ mm/s}$$

$$a_{\text{opt}} = 0.1 \text{ mm/s}^2$$

Further cutting parameters and evaluation are discussed in later sections.

Motor’s Backlash Correction

Another challenge addressed in the software is the motors’ backlash correction. As previously mentioned, the motors exhibit a backlash of approximately $1 \mu\text{m}$, meaning the motor’s reported position may differ from the actual position when reversing direction. This creates asymmetric positional errors. Backlash in stepper motors arises due to mechanical play or looseness in the drivetrain components (such as gears, lead screws, or couplings) that causes a delay or gap when changing direction. This results in a small, temporary loss of motion precision as the system takes up the slack before the motor’s movement fully translates to the load.

To correct for this, the software tracks the direction of the last movement for each motor and applies an offset to compensate. In symmetric back-and-forth movements, the error cancels out, but otherwise, correction is necessary. Since backlash can vary

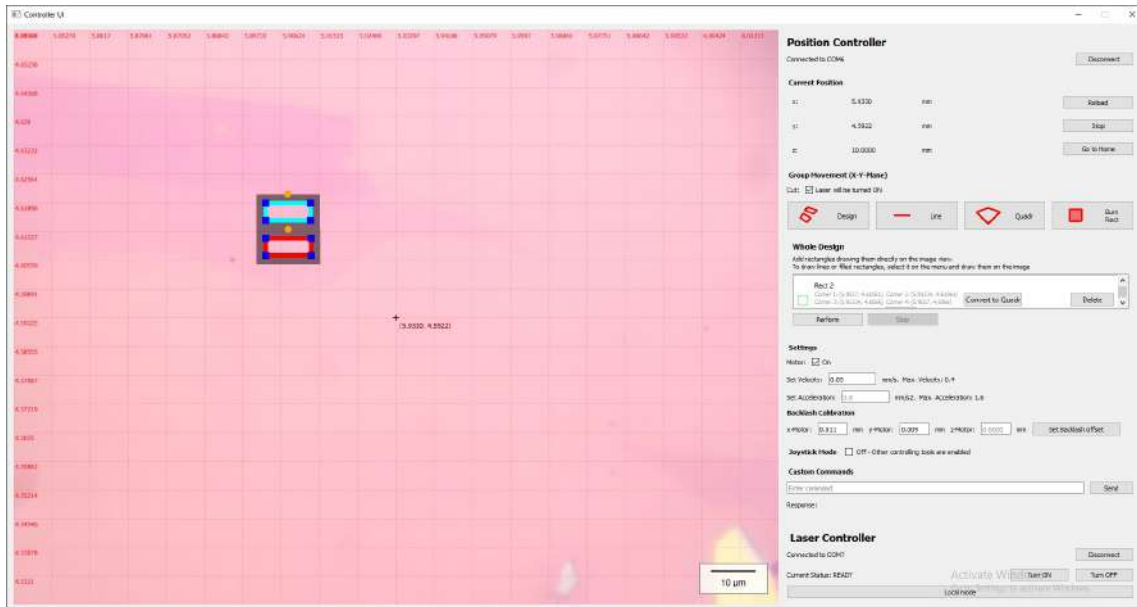


Figure 3.8: Example of a cutting design overlaid on a graphene flake, illustrating how rectangles and deletion areas are defined before execution.

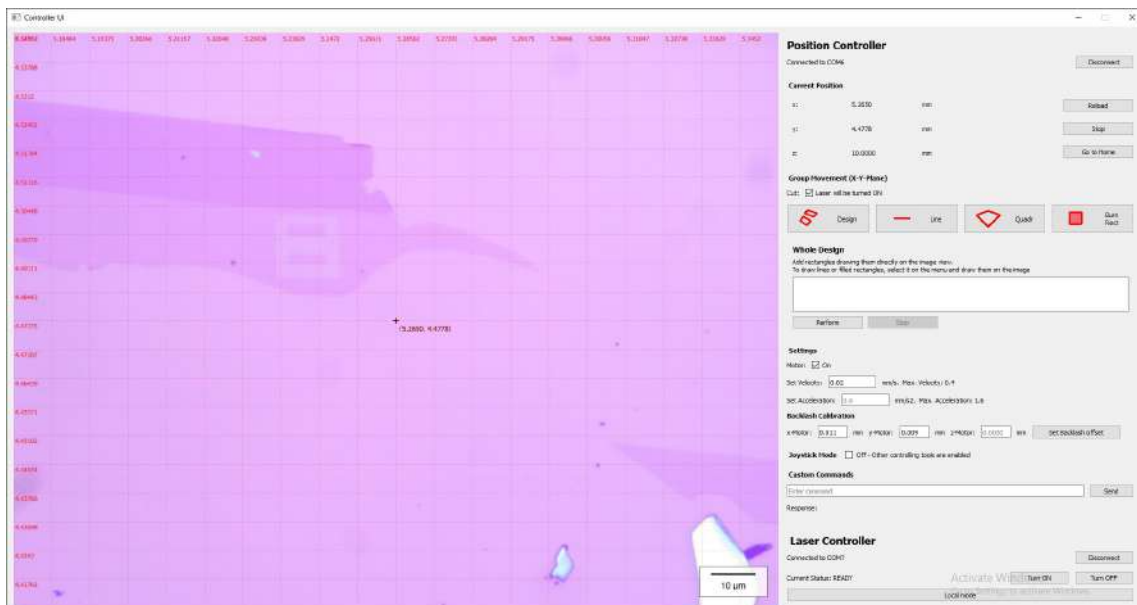


Figure 3.9: Camera image of the same graphene flake after the laser-cutting process, showing the successfully isolated regions. A different objective optimized for visible light was used for this image to improve visualization.

Backlash Correction

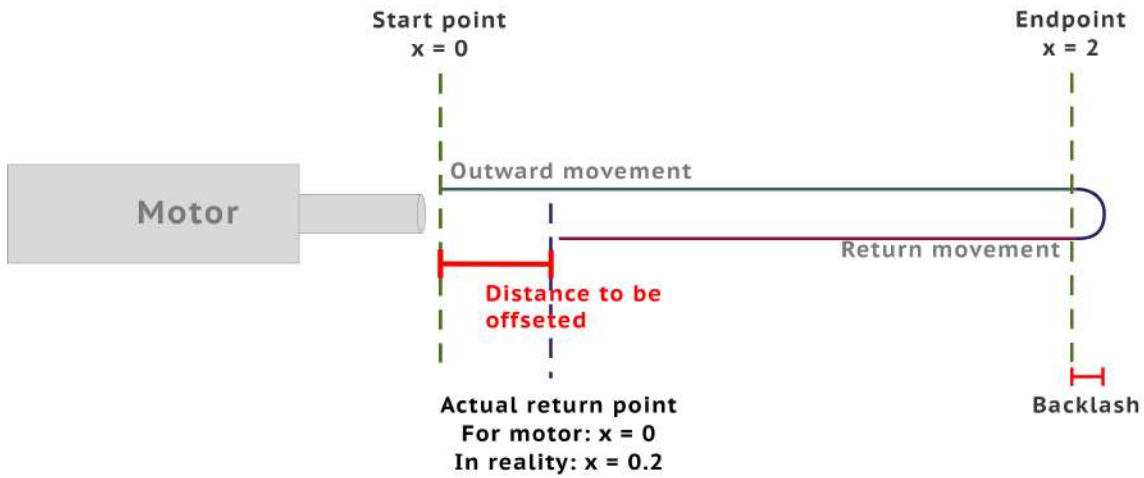


Figure 3.10: Schematic representation of motor backlash correction. The offset compensates for mechanical play in the motor gears when changing movement direction.

depending on the motor and over time, the GUI provides text fields to adjust the offset values. Users should re-calibrate these offsets after extensive movements or if positioning becomes unreliable.

The simplest way to determine the correct offset — used throughout this thesis — involves moving a certain distance along one axis from the center of a calibration cross (see Fig. 3.5) and then returning. The displacement between the start and end points represents the required correction.

3.2 Optical Microscopy

The exfoliated graphene flakes with different numbers of layers were first analyzed using optical contrast. A Nikon Eclipse LV150NA optical microscope, together with its imaging software NIS-Elements, was used to evaluate the change in green-channel intensity between the bare SiO_2/Si substrate and the regions covered by graphene flakes.

Based on the calibration, the approximate intensity drop per graphene layer was found to be around 10 intensity units. This relationship is illustrated in Figure 3.11, which shows the intensity profiles for tetra-, tri-, and bilayer graphene regions.

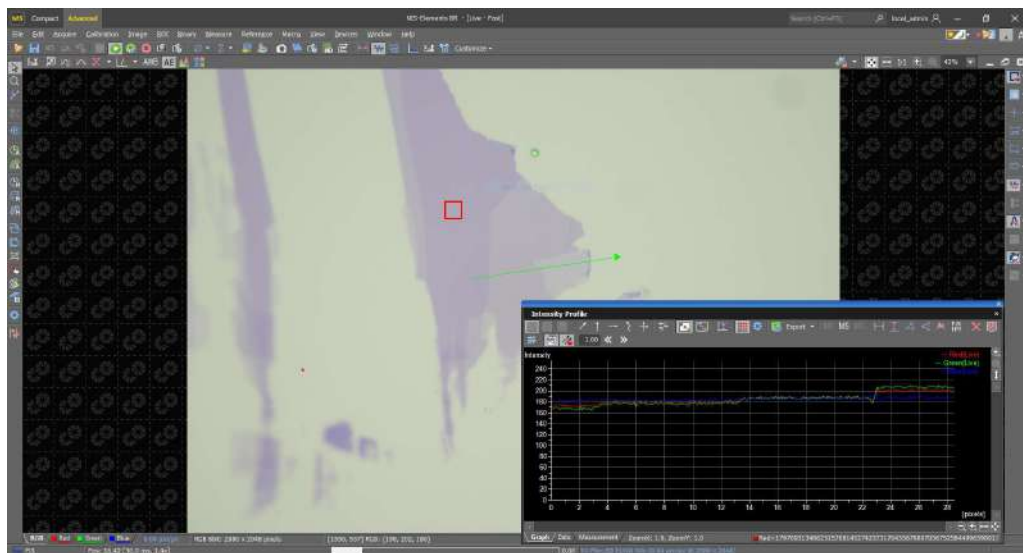


Figure 3.11: Intensity profile measurements of exfoliated graphene flakes, used to identify the number of layers based on optical contrast variations, measured using NIS-Elements software. Showing tetra-, tri-, and bilayer graphene regions.

Chapter 4

Results and Discussion

The experimental approach described in Chapter 3 enabled a comprehensive investigation into the laser-induced ablation behavior of graphene. In this chapter, the results of these experiments are presented, focusing on how key variables such as the number of graphene layers, irradiation time, and scanning parameters influence the damage threshold and cutting quality. The results are interpreted in the context of thermal transport, phonon behavior, and the unique dimensional characteristics of two-dimensional materials.

4.1 Damage-Threshold Graphene

Once the microscope was built and both single-layer and multilayer graphene could be successfully ablated, it became evident that this setup could be used not only for etching and fabrication, but also for an in-depth analysis of the ablation process itself—specifically, how the damage threshold depends on parameters such as exposure time, the number of layers, and cutting speed.

4.1.1 Layer-Dependent Damage Threshold

The question of the layer-dependent damage threshold—i.e., the fluence required to create a hole in different numbers of graphene layers—is particularly interesting, as it directly relates to the two-dimensional nature of graphene. [63] [64]

In this experiment, various flakes consisting of one to four graphene layers, identified using optical microscopy, were irradiated with the laser for **2 s** at different power levels. The acquired data can be extracted from C.1.

Fluence was calculated using a laser spot size of $1.33\ \mu\text{m}$, measured via its average pixel size in the camera image.

Controlling the Power with Two Polarizers

A critical part of the experiment was the ability to vary the laser power despite its fixed output. This was achieved using a pair of linear polarization filters. As

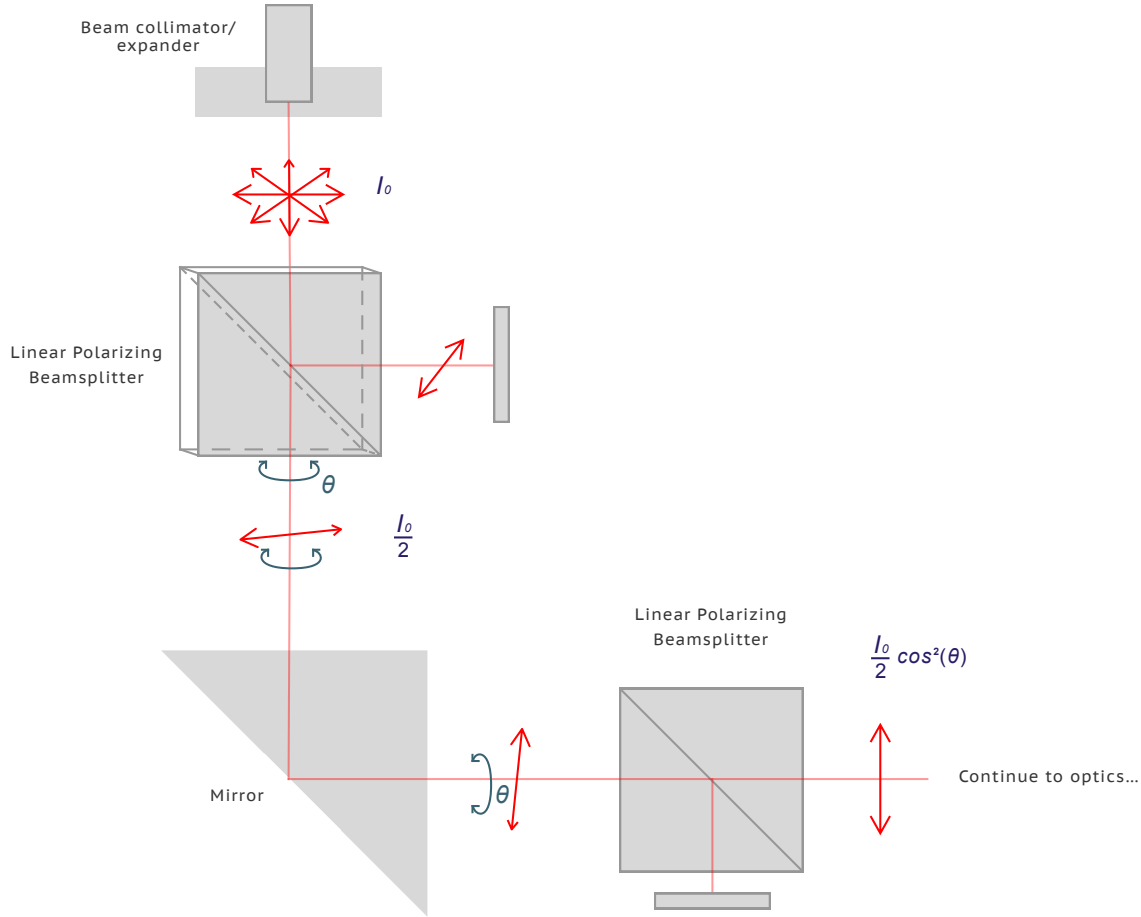


Figure 4.1: Schematic of the polarizer setup used to adjust the laser power via controlled polarization rotation.

shown in Fig. 4.1, the filters were placed in the optical path of the laser. The power transmitted through two linear polarizers rotated by an angle θ is given by Eq. (4.1) [65]. This setup allowed continuous tuning of the laser power across the range of interest. The precise power between the polarizers did not need to be calculated, as the power after the second filter was measured before each data point acquisition.

$$P_2 = \frac{P_0}{2} \cos^2 \theta \quad (4.1)$$

Between the power measurement point and the sample (as Fig. 4.1 shows), the beam passed through several optical components, including the dichroic mirror and objective lens, which significantly attenuated the light. This means that the measured power does not correspond to the actual power that arrives at the sample. The power had to be corrected for average losses. To quantify this loss, power measurements were taken before and after these optics after all the main experiments were done. Measuring losses at every data point would have introduced inconsistencies due to the movement of the stage and refocusing, so the same focal and alignment conditions were maintained throughout the dataset. All fluence values presented here account for this average power loss.

Fig. 4.4 illustrates how the number of remaining layers depends on the fluence. It is assumed that each flake was either fully ablated (zero layers remaining) or

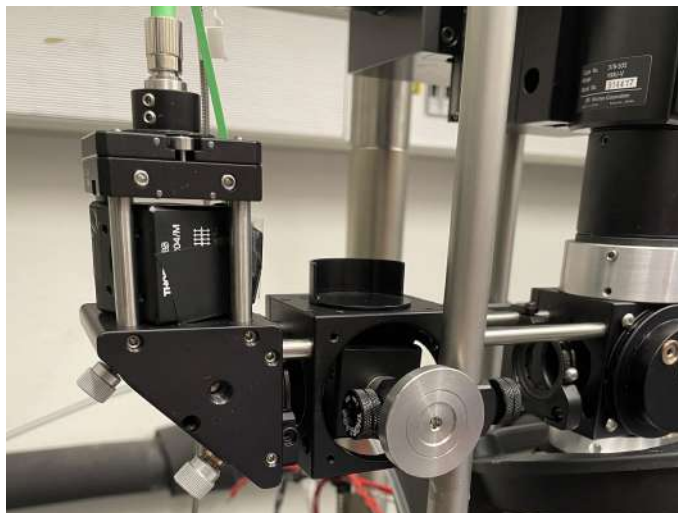


Figure 4.2: Photograph of the actual polarizer arrangement integrated into the laser's optical path, enabling precise power control for ablation studies.

unaffected. Thus, the last fluence value that did not lead to ablation was defined as the **damage threshold fluence**.

The laser power was recorded, and the remaining number of graphene layers after 2s of irradiation was determined using AFM.

Evaluation of Laser-Induced Damage

A key challenge was determining whether the sample was damaged. Initially, this was done visually under the microscope, which proved inconsistent—especially for thinner flakes, where optical contrast was low. In some cases, damage visible shortly after irradiation disappeared later, likely due to fluorescence effects or other unexplained phenomena.

To address this, AFM in tapping mode was used for thinner flakes. This method provided consistent identification of damage without requiring high-resolution images. AFM phase data was used due to better contrast. As shown in Fig. 4.3, irradiated regions with varying fluence exhibit increasingly less visible damage, disappearing entirely below a threshold. The last fluence at which damage was still visible was taken as the damage threshold for that number of layers.

Error Calculation

As with any experimental process, the results are subject to measurement errors. The combined uncertainty in the fluence was estimated using Gaussian error propagation. The measured values and uncertainties used in this calculation are as follows:

$$D = (1.33 \pm 0.10) \mu\text{m} \quad (\text{Laser spot diameter})$$

$$P_{\text{loss}} = (53.1 \pm 0.8) \% \quad (\text{Power loss through optics})$$

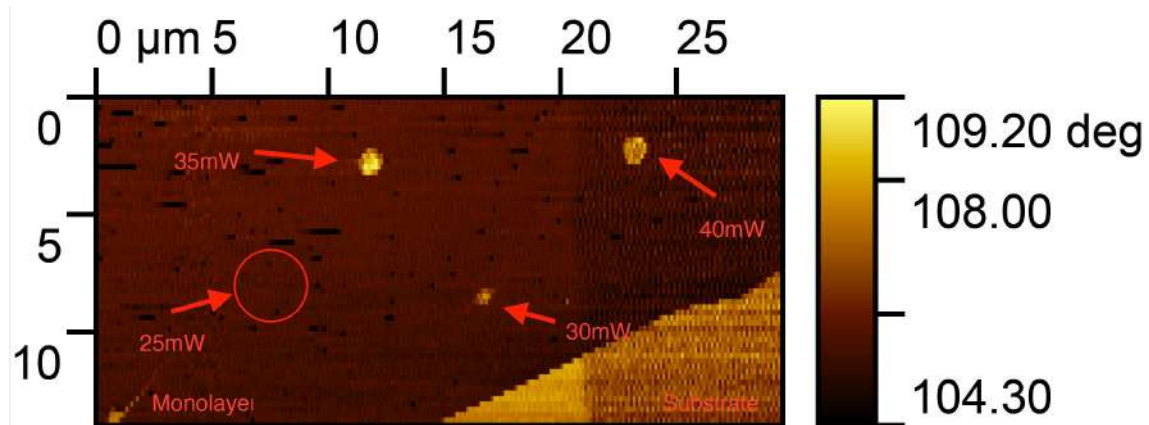


Figure 4.3: AFM (Phase) of monolayer damage. The phase data was used due to improved contrast. Different damage points are recognizable: irradiation with 40 mW, 35 mW, and—less visibly—30 mW. At the location irradiated with 25 mW, no damage is recognizable.

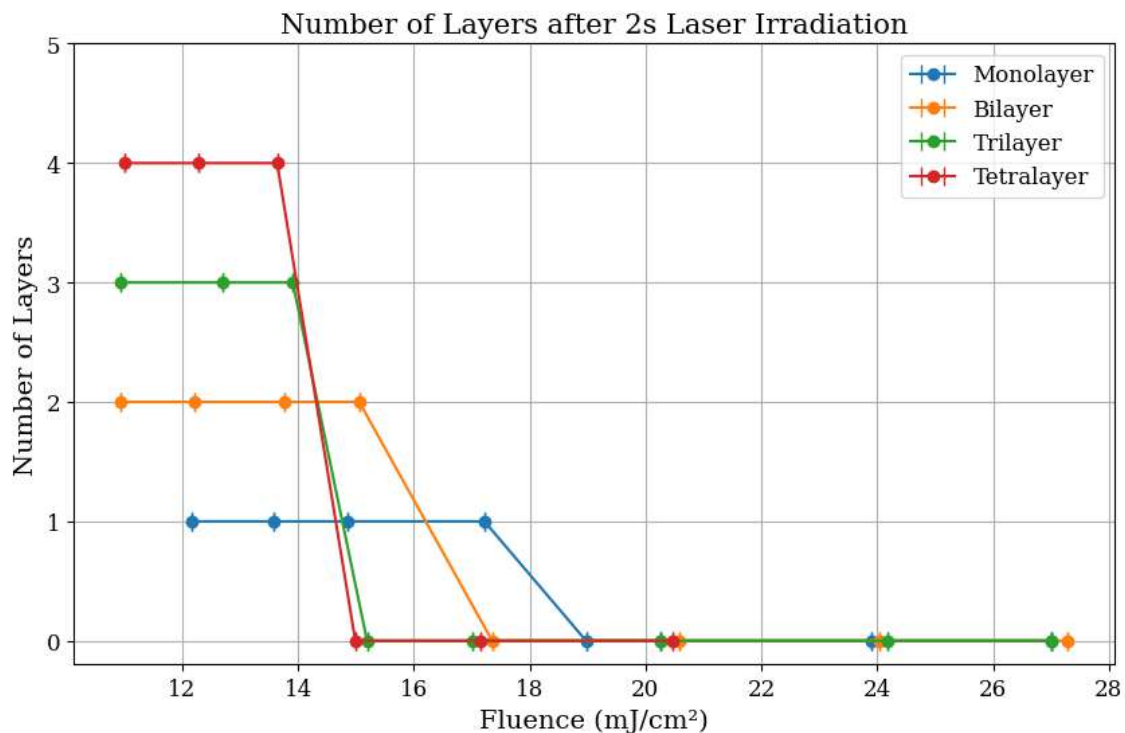


Figure 4.4: Remaining number of graphene layers plotted against fluence after 2 seconds of irradiation. The figure shows that a higher number of layers requires less fluence to be ablated.

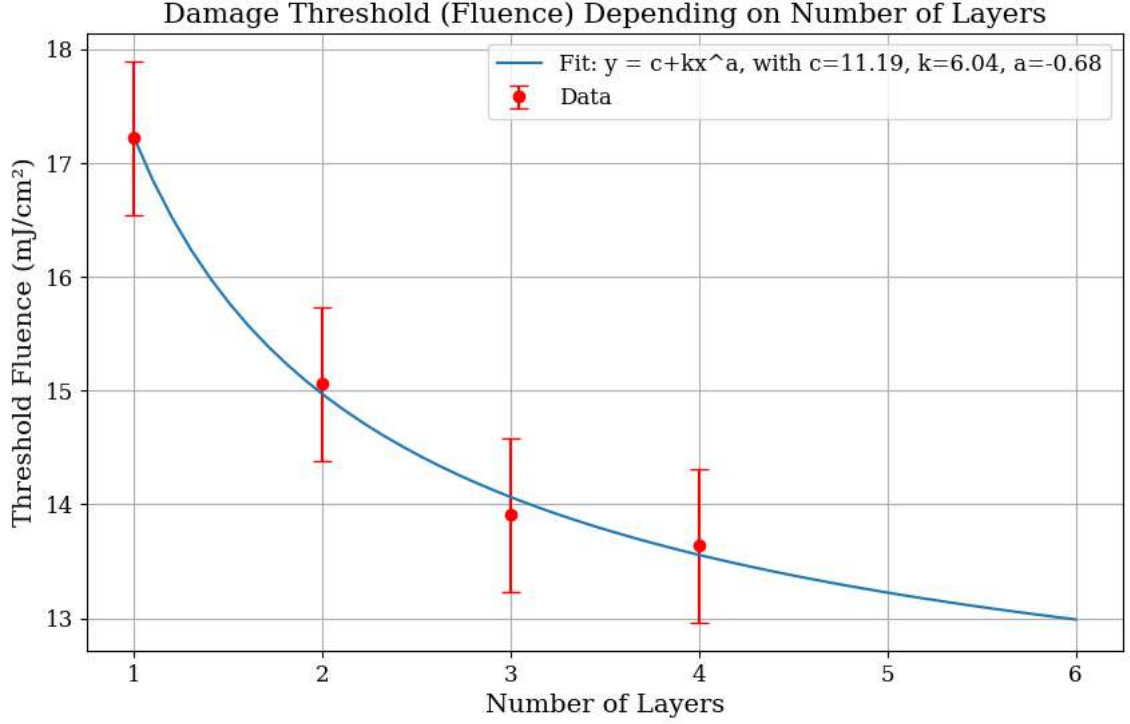


Figure 4.5: Layer-dependent ablation threshold fluence. The threshold decreases with increasing layer number and approaches saturation for multilayer graphene, confirming the strong influence of dimensionality on thermal transport.

$$\Delta P = 1.0 \text{ mW} \quad (\text{Power measurement uncertainty})$$

These yield the following general expression for the uncertainty in fluence:

$$\Delta F = \sqrt{\left(\frac{\partial F}{\partial P} \Delta P\right)^2 + \left(\frac{\partial F}{\partial P_{\text{loss}}} \Delta P_{\text{loss}}\right)^2 + \left(\frac{\partial F}{\partial D} \Delta D\right)^2} \quad (4.2)$$

$$F(P) = \frac{P(1 - P_{\text{loss}})}{f \cdot \pi \left(\frac{D}{2}\right)^2} \quad (4.3)$$

where f is the laser frequency.

Fig. 4.5 presents the damage threshold fluence as a function of layer number, including error bars. Since no adjustments were made to the focal position or optics throughout the experiment, systematic uncertainties (e.g., spot size) merely shift the data along the x-axis but do not affect the relative dependence across samples. This means that when comparing the layers (not absolute values), the uncertainty reduces to:

$$\Delta F = \sqrt{\left(\frac{\partial F}{\partial P} \Delta P\right)^2 + \left(\frac{\partial F}{\partial P_{\text{loss}}} \Delta P_{\text{loss}}\right)^2} \quad (4.4)$$

Fitting and Interpretation of Parameters

As previously illustrated in Fig. 4.4, the ablation threshold decreases with an increasing number of layers, approaching a saturation value captured by the fit parameter c . The parameter a was introduced to keep the relationship as general as possible and to avoid drawing overly specific conclusions, given the limited number of data points and inherent measurement uncertainties.

Despite the data limitations, the fit parameters—derived using the min-max error estimation method—allow for a meaningful physical interpretation:

$$c = (11.19 \pm 2.31) \text{ mJ/cm}^2 \quad (\text{Saturation threshold for thick samples}), \quad (4.5)$$

$$k = (6.04 \pm 2.27) \text{ mJ/cm}^2 \quad (\text{Baseline offset or calorimetric constant}), \quad (4.6)$$

$$a = (-0.68 \pm 0.40) \quad (\text{Layer-dependent scaling factor}). \quad (4.7)$$

Two key observations emerge from Fig. 4.5. First, and perhaps counterintuitively, **the fewer layers that are irradiated, the more difficult it becomes to induce ablation**. Second, **the damage threshold appears to saturate at a certain value as the number of layers increases**—particularly once the system leaves the two-dimensional (2D) regime (Fig. 4.6).

Intuitively, one might expect that fewer layers should require less energy to damage, since, as discussed in the theoretical background, the ablation process is largely driven by sublimation. More material (i.e., more layers) should imply a higher energy requirement due to the greater mass needing to be sublimated.

However, the energy that contributes to heating the material is determined by its ability to absorb light, and in the case of graphene, the absorption coefficient scales approximately linearly with the number of layers [7]. A simple energy balance equation helps clarify this point. The energy threshold per unit area E_{th} is given by:

$$E_{\text{th}} \cdot \alpha = mc_t \Delta T, \quad (4.8)$$

where α is the absorption, ΔT is the temperature increase required for sublimation, m is the mass per unit area, and c_t is the specific heat capacity.

The layer-dependent mass per unit area can be expressed as:

$$m(N) = \rho_{\text{graphite}} \cdot h \cdot N \quad \Rightarrow \quad m \propto N, \quad (4.9)$$

where $h = 0.34 \text{ nm}$ is the height of a single graphene layer. Similarly, as described earlier, the absorption scales as [7]:

$$\alpha \propto 0.023 \cdot N. \quad (4.10)$$

Substituting these relations and introducing a constant C_0 into the energy balance yields:

$$E_{\text{th}} = C_0 \cdot \frac{Nc_t}{0.023N}, \quad (4.11)$$

which implies that the fluence threshold is also governed by the layer-dependent specific heat capacity c_t . In bulk materials, c_t is often treated as a constant, but this assumption breaks down in 2D materials like graphene. The specific heat capacity has a direct relation to the thermal conductivity [28], and as shown in [28] [22], monolayer graphene has a higher in-plane thermal conductivity than multilayer graphene. Since the ablation process involves rapid local heating [66] [20] (more rapid than the heat can diffuse laterally), higher thermal conductivity can hinder the temperature rise necessary for sublimation.

This interpretation aligns with the explanation proposed by *Dhar et al.* [9] (as described in the theoretical background), who attribute the specific heat capacity in few-layer systems primarily to flexural phonons [28], which can be excited by a laser beam [67]. They derive the following expression for the specific heat capacity of an N -layer graphene system [9]:

$$c_f(N, T) = \frac{\pi}{12} \sqrt{\frac{\rho}{Y}} \frac{k_B^2 T}{c} \cdot \frac{1}{N}, \quad \text{thus } c_f(N, T) \propto \frac{1}{N}, \quad (4.12)$$

where ρ is the density of graphite, Y the Young's modulus, k_B the Boltzmann constant, T the temperature, and $c = 0.34$ nm the interlayer distance [9]. Substituting this into Eq. 4.11 yields:

$$E_{\text{th}}(N) = E_\infty + \frac{k}{N}, \quad (4.13)$$

where E_∞ represents the threshold fluence in the bulk (i.e., 3D) limit and k is a constant. This $1/N$ dependence matches (within the scope of error) the experimental fit to the data in Fig. 4.5.

It must be noted, however, that the experimental setup used in this study introduces a distinct thermal environment compared to single-shot laser ablation experiments in the literature. In particular, the long irradiation times (on the order of seconds) lead to significant heat accumulation and possible thermal interaction with the substrate [20]. The underlying SiO_2/Si substrate has relatively low thermal conductivity, which could act as a heat reservoir [68]. Although out-of-plane heat transfer in graphene is limited [3], heat absorbed by the substrate may feed back into the graphene layers, especially since graphene's absorption still scales with layer number.

Given the limitations of the dataset and the complexity of disentangling overlapping physical mechanisms, these conclusions must be considered tentative. Nevertheless, the data clearly support the qualitative conclusion that the fluence threshold in the few-layer regime decreases approximately as $1/N$ and gradually saturates as the number of layers increases. This behavior arises from the combined effects of increasing absorption, decreasing in-plane thermal conductivity, and phonon-mode contributions to heat capacity in ultrathin systems.

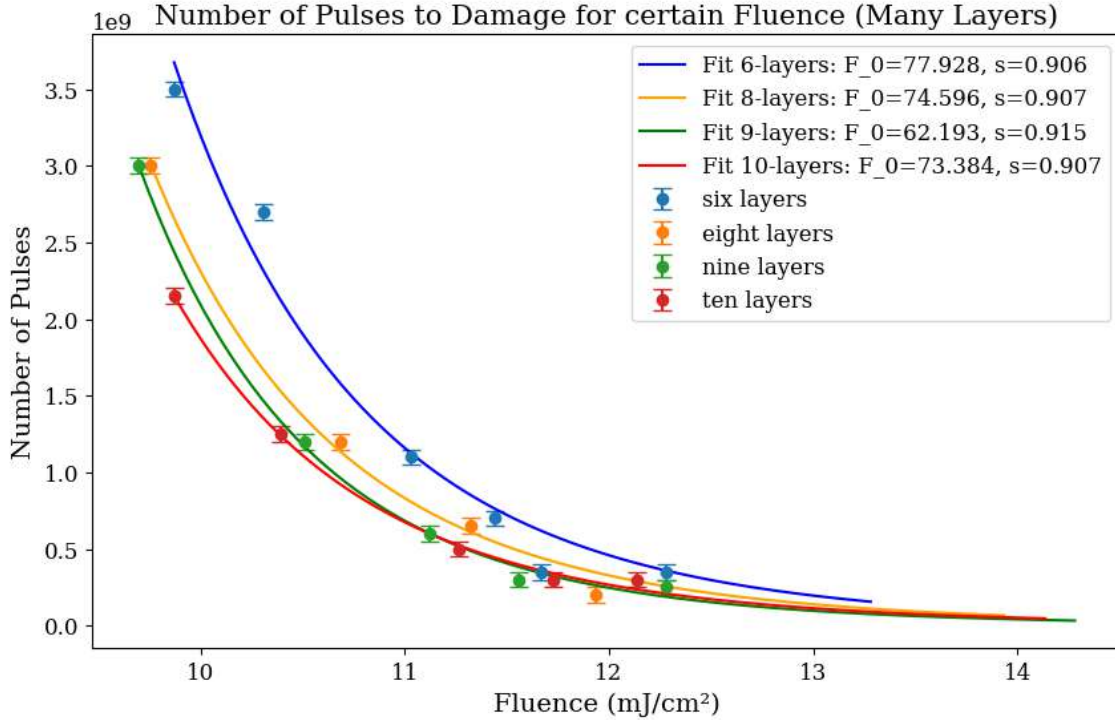


Figure 4.6: Number of pulses required for ablation at different fluences for multilayer graphene. The data demonstrate a clear incubation effect, where longer exposure times reduce the required fluence.

4.1.2 Time-Dependent Damage Threshold

All measurements discussed so far were conducted with an irradiation duration of approximately 2 s. This time frame results from the operational protocol: turning the laser on, waiting one second, and then turning it off yields an effective exposure time of about two seconds. While this setup does not permit the investigation of single-pulse phenomena, it is nonetheless suited to studying the damage threshold as a function of irradiation time in the multi-second regime. In particular, it allows for the determination of how the fluence required to damage graphene changes with exposure duration.

The measurement method followed the procedure established in the previous section: a fixed fluence was used to irradiate a flake for a defined duration. If the flake was visibly damaged, a new region of the same flake was exposed for a shorter time; if no damage occurred, the exposure time was increased. This iterative process was repeated until the damage threshold time was determined with a temporal resolution of approximately 2 s.

Two sets of samples were analyzed. For multilayer flakes (6–10 layers), optical microscopy was sufficient for detecting damage due to the elevated contrast. For few-layer flakes (1–4 layers), atomic force microscopy (AFM) was employed due to the limited optical contrast and the difficulty of visual identification. The results are presented in Figs. 4.6 and 4.9. Although time constraints limited the number of data points for few-layer samples, clear trends were still identifiable.

Due to differences in experimental setup and calibration, the multilayer data were

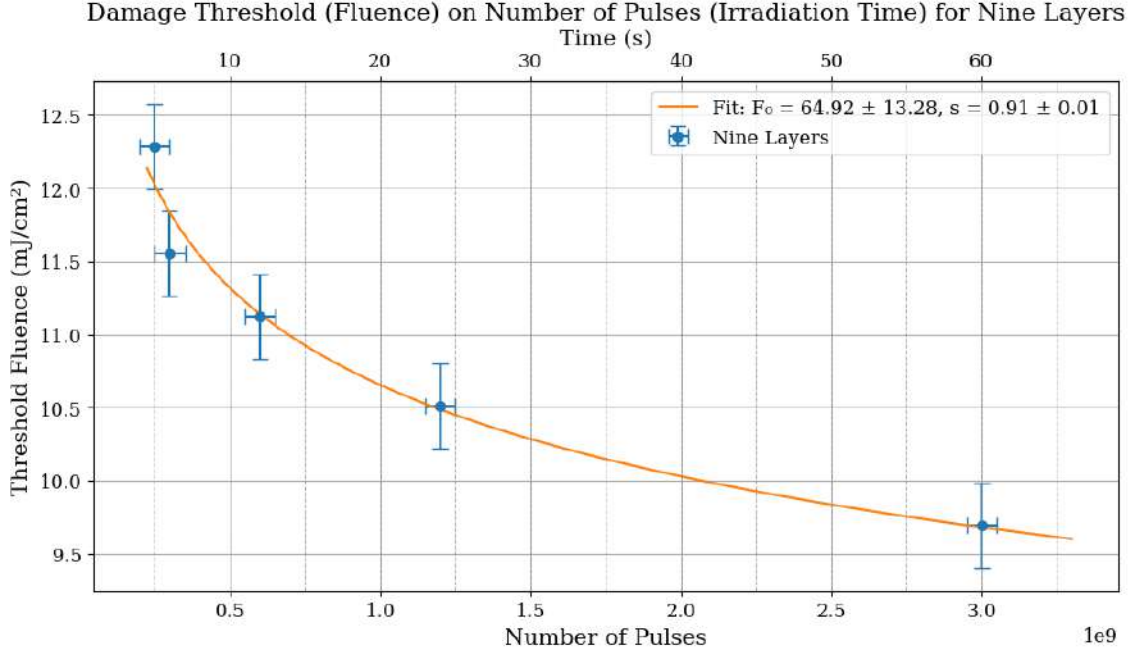


Figure 4.7: Threshold fluence versus exposure time for 9-layer graphene. The threshold fluence drops with increasing exposure time, illustrating cumulative thermal effects during multi-second irradiation.

scaled by a correction factor to align with the few-layer results.

As outlined in the theoretical background, the fluence threshold as a function of the number of laser pulses follows a power-law behavior [23][8]:

$$F(N) = F_0 \cdot N^{s-1} \quad (4.14)$$

where $N = t \cdot f$ is the number of pulses, F_0 is the single-pulse damage threshold, and s is the incubation coefficient [69]. Fig. 4.6 shows this relation for multiple thicknesses, while Fig. 4.7 focuses specifically on the threshold fluence versus exposure time for the 9-layer sample.

For the 9-layer flake, the extracted fit parameters are:

$$F_{0,\text{exp}}^{9\text{-layers}} = (64.92 \pm 13.28) \text{ mJ/cm}^2 \quad (4.15)$$

$$s = 0.91 \pm 0.01 \quad (4.16)$$

The obtained F_0 lies below the monolayer threshold discussed in Sec. 4.1.1, consistent with the expected trend that thicker flakes require less fluence per pulse due to thermal accumulation effects.

Moreover, the exponent s is compatible with previously reported values for nanosecond laser ablation in 2D materials ($s \approx 0.88$) [8], further supporting the thermal incubation model. Errors were estimated using the min-max method.

As shown in Fig. 4.8, the number of remaining layers after irradiation depends on fluence and exposure time. For example, for $t_1 = 2$ s, the threshold fluence is approximately 17.2 mJ/cm^2 , while for $t_2 = 5$ s it decreases to around 13.6 mJ/cm^2 .

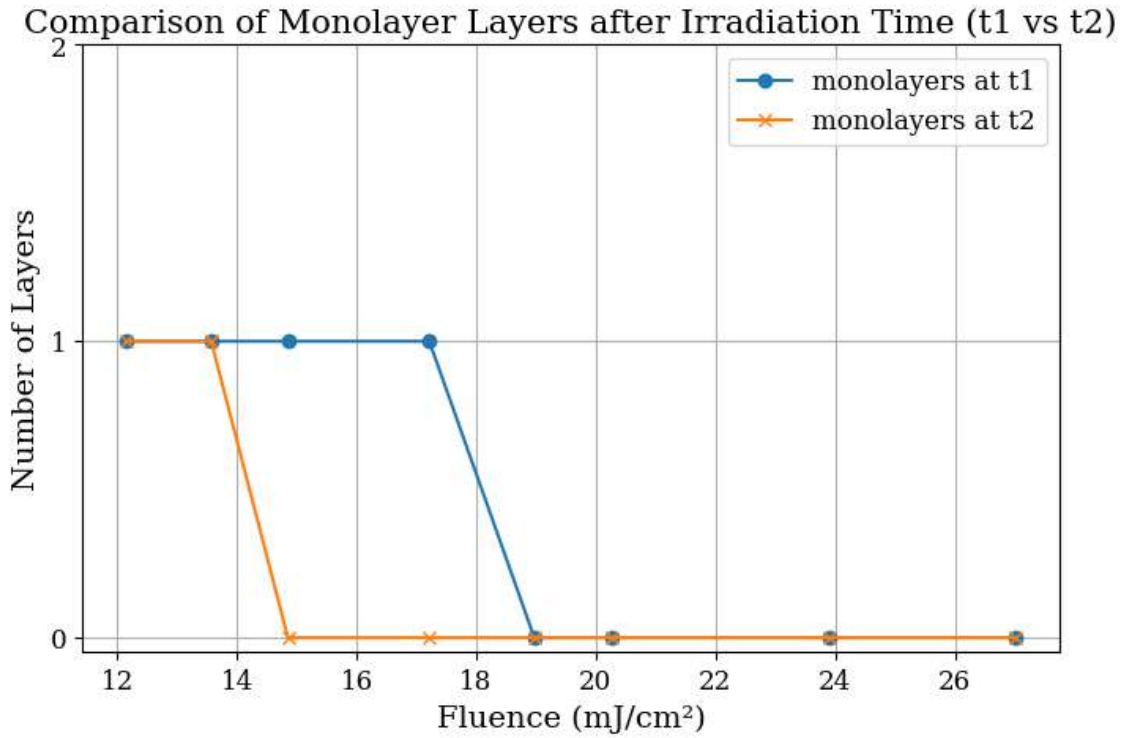


Figure 4.8: Number of layers of a monolayer flake as a function of the damage threshold at different irradiation times. The comparison between $t_1 = 2$ s and $t_2 = 5$ s demonstrates that longer irradiation times significantly reduce the threshold needed to induce damage in graphene.

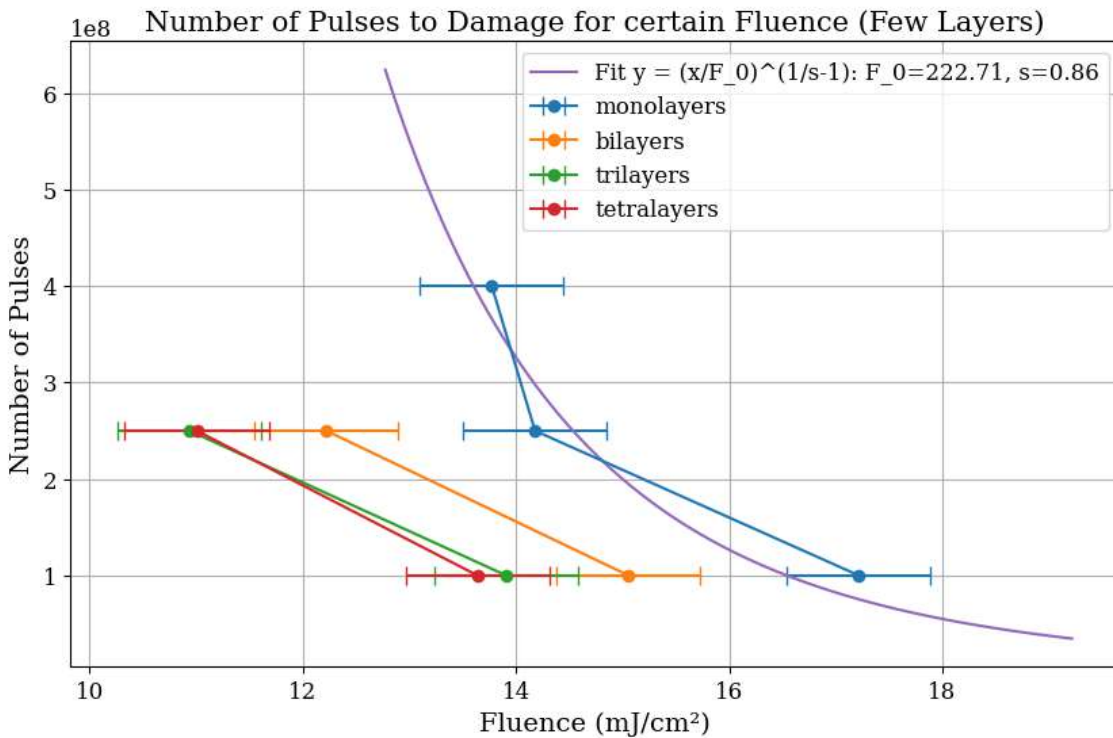


Figure 4.9: Time-dependent ablation thresholds for few-layer graphene. The data can show a power-law decrease in threshold fluence with pulse count, consistent with incubation models from the literature.

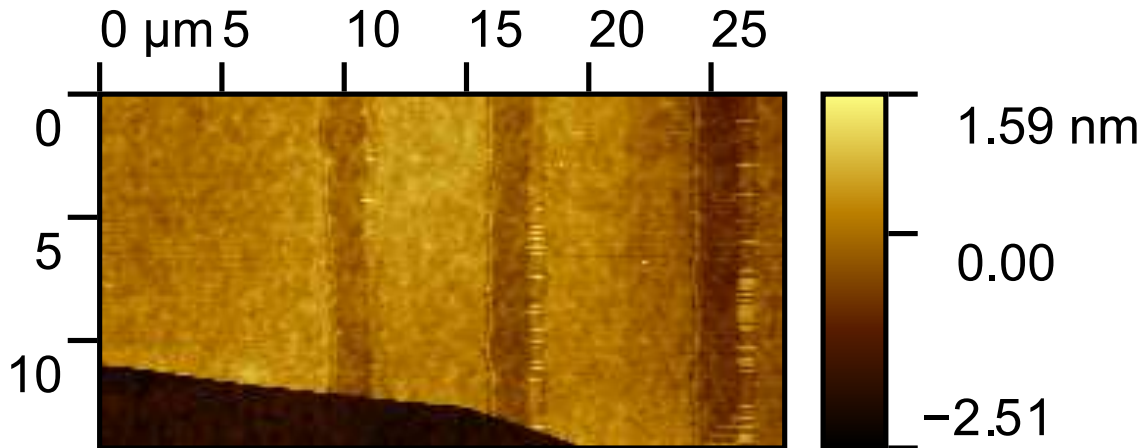


Figure 4.10: AFM image of monolayer graphene cuts performed at decreasing scan speeds (left to right). Slower scanning results in wider cuts due to longer local exposure and increased thermal diffusion. The speeds are: 0.1 mm/s, 0.01 mm/s, and 0.001 mm/s.

This time-dependent reduction in threshold fluence for monolayer graphene follows a power-law trend (Fig. 4.9) with an exponent consistent with previous experimental results [8] and a F_0 value close to the previously determined single-pulse ablation threshold with similar lasers [26][23].

Although limited in data points, these measurements robustly confirm that damage threshold decreases with increasing pulse count—an outcome of cumulative heating effects. However, given the constraints of data quality and quantity, extracted values should be interpreted cautiously.

4.1.3 Analysis of Cuts

In comparison to the graphene damage threshold studied previously, the cutting process involves a dynamic scenario in which the laser moves continuously across the sample. As a result, no single point is irradiated for the full duration of 2 s used in threshold measurements. To achieve effective cutting within the brief period that each point is exposed, the delivered power must be higher. This, of course, depends on the scanning speed: the slower the laser moves, the longer each point is irradiated. Notably, the central part of each cut line typically receives the most exposure due to the beam’s Gaussian intensity profile as well.

While slower scanning speeds provide longer irradiation and thus improve cutting reliability, they also tend to produce less clean cuts due to prolonged thermal effects and heat diffusion into the surrounding material. This relationship was investigated using single-layer graphene at a fixed laser power of 100 mW, where three linear cuts were performed at different speeds: 0.1 mm/s, 0.01 mm/s, and 0.001 mm/s. The resulting flake was analyzed via atomic force microscopy (AFM), as shown in Fig. 4.10, where the cuts progress from left to right in decreasing speed.

As can be observed, slower speeds result in wider cuts due to increased exposure. This effect is more clearly visualized in the extracted profiles of each cut, shown in

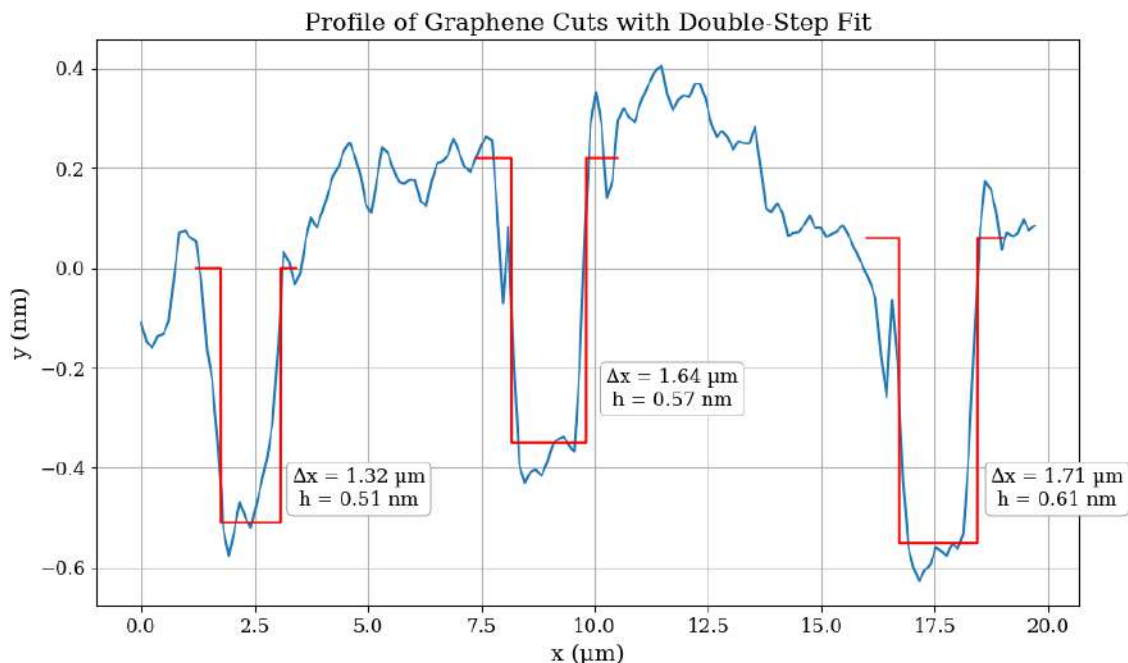


Figure 4.11: Profiles of the three line cuts at different speeds. The width increases with slower speeds, indicating prolonged thermal interaction.

Fig. 4.11. The profile demonstrates how cut width increases with longer irradiation time. Interestingly, the narrowest cut—achieved at a speed of 0.1 mm/s—has a width approximately matching the laser spot diameter, consistent with values calculated earlier in this thesis.

The results are:

$$\begin{aligned}
 v = 0.1 \text{ mm/s} & \quad \Rightarrow w = 1.32 \text{ } \mu\text{m} \\
 v = 0.01 \text{ mm/s} & \quad \Rightarrow w = 1.64 \text{ } \mu\text{m} \\
 v = 0.001 \text{ mm/s} & \quad \Rightarrow w = 1.71 \text{ } \mu\text{m}
 \end{aligned}$$

The step height for the first cut corresponds closely to the known height of a monolayer graphene sheet:

$$h = (0.51 \pm 0.07) \text{ nm} \quad (4.17)$$

Additional cuts were performed at reduced laser powers of 85 mW and 75 mW. These were analyzed optically. As expected, at lower powers, the fast cuts became increasingly faint or even invisible, while slower cuts remained detectable. This behavior further confirms the role of both power and dwell time in achieving successful ablation.

4.2 Cutting hBN-Encapsulated Graphene

Motivated by potential applications and scientific curiosity, an experiment was conducted to evaluate whether hBN-encapsulated graphene can be ablated using the laser setup described in the previous sections.

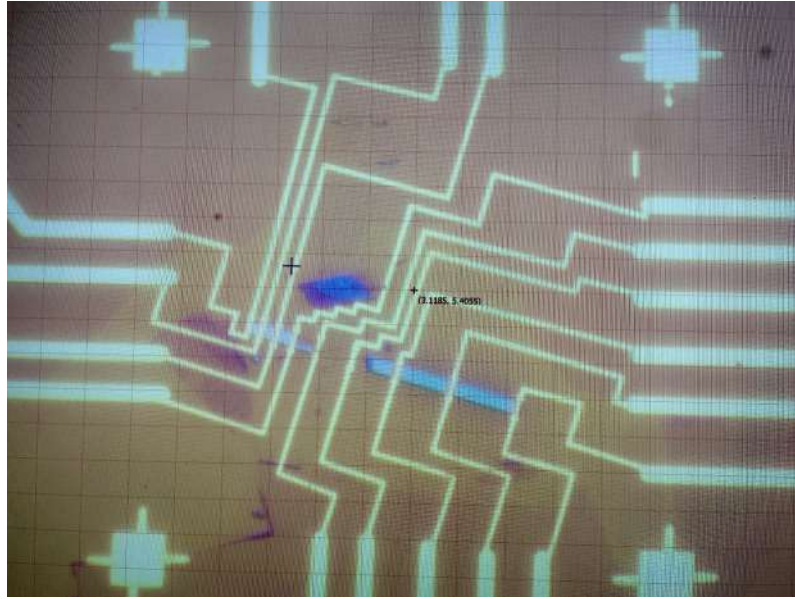


Figure 4.12: Optical microscope image of hBN-encapsulated graphene device with gold contacts before laser exposure. This configuration was used for subsequent conductivity measurements during laser irradiation.

The primary difference between bare and encapsulated graphene lies in the interaction of the laser with the material: in encapsulated structures, the laser irradiates the top hBN layer, not the graphene directly. As illustrated in Fig. 4.12, the encapsulated flake features gold contacts for conductivity measurements. According to the theoretical background, hBN is an electrical insulator with a wide band gap, implying that the energy delivered by the laser should, in principle, pass through the hBN and reach the underlying graphene without significant absorption.

A series of test cuts were performed by varying the scanning speed of the motorized stage. The sample was irradiated at speeds ranging from 0.1 mm/s to 0.001 mm/s. After each irradiation step, electrical conductivity was measured using a vacuum probe station (Fig. 4.13).

No change in conductivity was observed in any of the initial trials. Subsequently, a longer exposure was applied: the laser irradiated the same region for approximately three minutes. Again, no noticeable change in conductivity occurred. Finally, the sample was exposed for over five minutes, with the laser scanned across the full width of the encapsulated graphene region, including its edges. After this step, a drop in conductivity was detected, reaching the minimal measurable conductivity of the system (Fig. 4.14).

Optical analysis after the final exposure revealed visible damage (Fig. 4.15) that was not present before irradiation (cf. Fig. 4.12). However, due to the optical opacity of the top hBN layer, the graphene beneath cannot be directly observed using standard optical microscopy. Therefore, the observed changes likely correspond to damage in the hBN itself.

Based on this observation, it is plausible that the change in conductivity stems not from simple graphene ablation but from structural alterations to the hBN layer or the substrate. As discussed in the theoretical background, graphene ablation

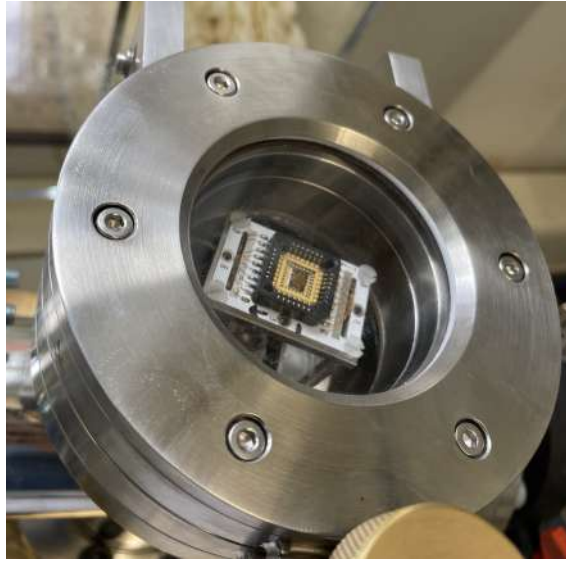


Figure 4.13: Vacuum probe station setup used for in-situ electrical conductivity measurements during laser irradiation of the encapsulated samples.

Electrical Conduction of Encapsulated hBN-Graphene under Laser Irradiation

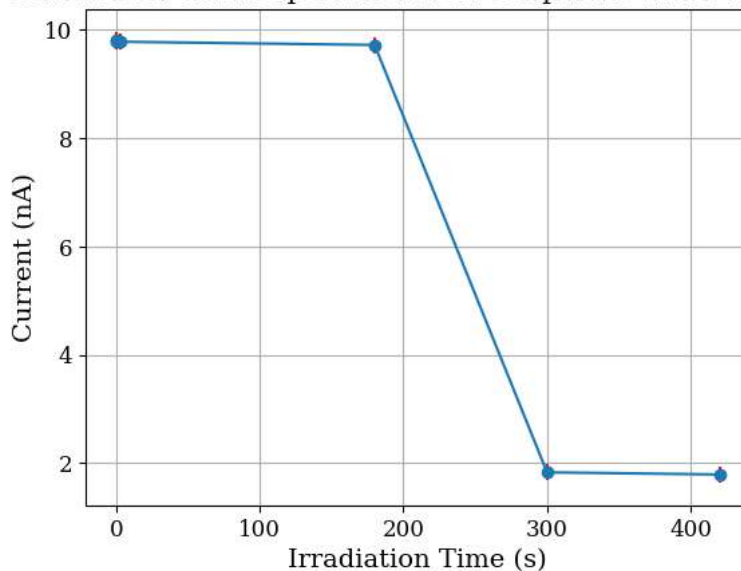


Figure 4.14: Conductivity of hBN-encapsulated graphene as a function of irradiation time. Conductivity remains stable during short exposures but drops sharply after prolonged irradiation, indicating delayed damage mechanisms. The conductivity reflects whether the graphene has been cut (non-conductive) or remains (conductive).

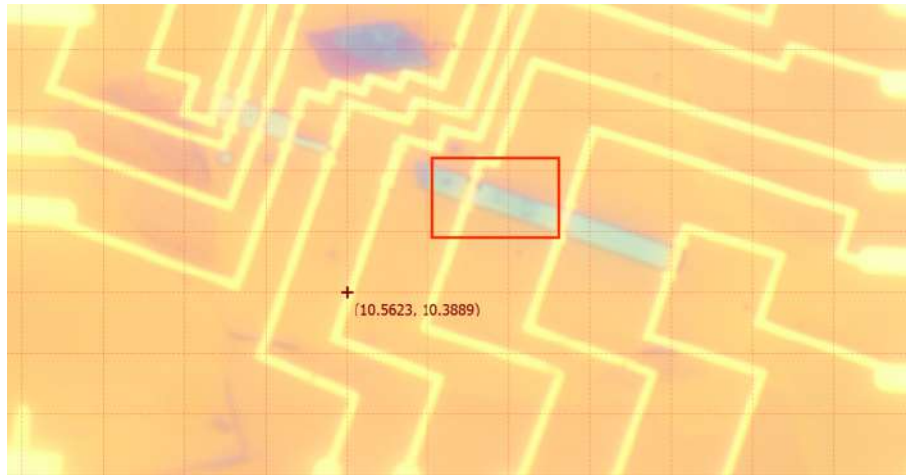


Figure 4.15: Optical image of the encapsulated sample after prolonged laser exposure. Visible damage on the hBN surface corresponds to the drop in conductivity, suggesting structural changes in the encapsulation layer.

typically requires thermal sublimation or defect formation via oxidation. In the encapsulated structure, these mechanisms are impeded: sublimated carbon species cannot escape, and oxidative damage is suppressed due to the absence of ambient oxygen in the confined structure.

A potential explanation for the conductivity drop could involve mechanical or thermal disruption of the encapsulation layer, leading to partial delamination of the hBN from the graphene. This may allow sublimated material to escape or alter contact between the graphene and electrodes, thereby breaking electrical continuity. Furthermore, the long irradiation time may have induced a significant incubation effect, culminating in damage that indirectly affects the conductive pathway.

Another explanation could be subsequent heating of the graphene via its edges. At the border, graphene may sublime, potentially initiating a tunnel-like ablation path where the burning graphene “escapes” through the boundaries.

It is worth noting that a control experiment was conducted on a different section of the same encapsulated flake, where the graphene still showed conductivity even after ten minutes of irradiation. This reinforces the hypothesis that the observed drop in conductivity was due to localized structural effects (e.g., substrate or hBN detachment), rather than direct graphene ablation through hBN.

To better understand these results, further experiments should be carried out. In particular, the use of thinner hBN layers and improved imaging techniques (e.g., cross-sectional SEM or Raman spectroscopy) could help determine whether the laser energy penetrates through the hBN to ablate the graphene or whether the effect is mediated by encapsulation-related damage mechanisms.

Chapter 5

Conclusions

This thesis has presented the design, construction, and application of a custom laser-cutting microscope for the controlled ablation of graphene. By integrating imaging with laser micromachining, supported by a fully developed Python-based graphical user interface, the system allowed for both efficient device fabrication and fundamental investigations into the ablation dynamics of graphene under laser irradiation.

The systematic experiments conducted revealed several key insights into the layer- and time-dependent behavior of graphene during laser ablation. First, the threshold fluence required to induce damage in graphene was found to decrease with increasing layer number, following a roughly inverse relationship that approaches saturation for thicker samples. This counterintuitive trend can be explained by considering both the increasing light absorption with layer count and the decreasing in-plane thermal conductivity due to the suppression of flexural phonon scattering in multilayer structures. The experimental data agreed qualitatively with theoretical models that attribute specific heat and thermal transport in graphene to dimensional phonon effects, providing additional confirmation of the unique thermal behavior of two-dimensional materials.

Second, extended irradiation times demonstrated a significant incubation effect, whereby longer exposure at sub-threshold fluences cumulatively lowered the energy required for ablation. The extracted incubation coefficients from both few-layer and multilayer samples were compatible with previous studies on nanosecond and picosecond laser ablation, confirming that thermal accumulation is a dominant mechanism even in multi-second exposure regimes.

The analysis of the cutting process itself further demonstrated the importance of optimizing scanning speed and laser power to balance cutting precision and material integrity. Higher scanning speeds yielded narrower and cleaner cuts approaching the diffraction-limited spot size of the focused laser beam, while lower speeds led to wider ablation channels and introduced broader thermal effects.

Finally, initial investigations into the ablation of hBN-encapsulated graphene highlighted the complexity introduced by protective layers. While no damage to the graphene could be directly observed under standard conditions, prolonged irradiation eventually led to graphene's conductivity loss, likely resulting from material removal due to structural disruption of the hBN encapsulation. These results suggest

that while encapsulation provides protection under moderate irradiation, long-term exposure may initiate indirect pathways for material degradation, potentially involving mechanical delamination or localized heating effects at the flake boundaries.

Overall, the developed laser-cutting system proved to be a versatile and effective platform for both practical device fabrication and for probing the intricate physics of laser–graphene interactions. Although the number of data points collected in this study did not permit definitive scientific conclusions, the observations obtained support existing models of thermal transport, optical absorption, and ablation dynamics in graphene, and provide a solid foundation for further research. Future extensions of this work could involve the use of alternative encapsulation materials, shorter pulse durations, in-situ thermal characterization, and advanced imaging techniques such as cross-sectional SEM or Raman spectroscopy to better elucidate the underlying damage mechanisms in layered heterostructures. In addition, a more systematic experimental approach is required to acquire reliable data for a detailed analysis of layer- and time-dependent ablation thresholds in both single- and multilayer graphene. This includes dedicated studies in the single-pulse regime, as well as investigations on thicker multilayer samples using robust and consistent methods for damage evaluation.

Appendix A

GUI Code Structure and Python Scripts

A.0.1 GUI Widgets

The code for the GUI software is organized into multiple Python files. The main file, `gui.py`, executes the application by integrating all relevant software modules and user interface components. It incorporates widgets from `CameraView.py`, which contains the code responsible for acquiring camera data and handling mouse interactions with the image for design creation. Additionally, `gui.py` implements the user interface elements for both the Motor Controller and the Laser Controller.

Several frequently used widgets are placed in `helper.py` for organizational purposes. Furthermore, two custom modules have been developed to manage the laser and ESP301 motor controllers. These modules are initialized within `gui.py`.

A.0.2 Software Modules

To manage hardware communication and state within `gui.py`, two classes were implemented: `ESP301.py` and `NPILaser.py`. Both classes inherit from `QObject` (PyQt5) and encapsulate the essential functions while maintaining the current status of the controllers.

The `ESP301` class stores the current motor positions, offset values, motion directions, and relevant settings. It is responsible for managing serial communication, transmitting all necessary ASCII commands to the ESP301 motor controller.

Similarly, the `NPILaser` class handles laser operations such as turning the laser on and off, monitoring the laser's status, and performing necessary status checks.

The complete source code for the software is available in the following Git repository: [GUI Laser-Cutting Microscope](#).

A.0.3 Python Script for Layer-Dependent Threshold

```
1 import numpy as np
2 import matplotlib.pyplot as plt
```

```

3  from scipy.optimize import curve_fit
4
5  #Constants
6  freq = 50 * 10**6
7
8  #Errors
9  laser_spot_error = 0.1 #microm
10 power_error = 1 #mW
11 time_error = 1 #s
12
13 #Avarage power loss
14 avg_power_loss = 0.531 #Percentage
15 avg_power_loss_error = 0.008
16
17 laser_spot = 1.33 #microm
18
19 def transform_power_uncertainty(P): #From measured power to (reduced) fluence with
    ↪ error
20     P_red = P*(1-avg_power_loss)
21     laser_spot_cm = laser_spot*0.0001
22     laser_spot_error_cm = laser_spot_error*0.0001
23     A = np.pi *(laser_spot_cm/2)**2
24
25     F = P_red/(freq*A)
26
27     #Error (Gau )
28     dF_dP = (1-avg_power_loss)/(freq*A)
29     dF_dr = -P/(freq*A) #Reduction Error
30     dF_dD = -P_red*(np.pi * laser_spot_cm)/(2*freq*A**2) #Laser Spot error
31
32     dF = np.sqrt((dF_dP*power_error)**2 #+
33                 #(dF_dr*avg_power_loss_error)**2
34                 #(dF_dD*laser_spot_error_cm)**2
35                 )
36
37     return F, dF
38
39 #Data Layers
40 monolayer_power = np.array([40.0, 35.4, 30.0, 28.1, 25.5, 22.0, 20.1, 18.0])
41 monolayer_layers_t1 = np.array([0, 0, 0, 0, 1, 1, 1, 1]) #2s Irradiation
42 monolayer_layers_t2 = np.array([0, 0, 0, 0, 0, 0, 1, 1]) #5s Irradiation
43 monolayer_layers_t3 = np.array([0, 0, 0, 0, 0, 0, 1, 1]) #8s Irradiation
44
45 bilayer_power = np.array([40.4, 35.6, 30.5, 25.7, 22.3, 20.4, 18.1, 16.2])
46 bilayer_layers_t1 = np.array([0, 0, 0, 0, 2, 2, 2, 2]) #2s Irradiation
47 bilayer_layers_t2 = np.array([0, 0, 0, 0, 0, 0, 2, 2]) #5s Irradiation
48
49 trilayer_power = np.array([40.0, 35.8, 30.0, 25.2, 22.5, 20.6, 18.8, 16.2])
50 trilayer_layers_t1 = np.array([0, 0, 0, 0, 0, 3, 3, 3]) #2s Irradiation
51 trilayer_layers_t2 = np.array([0, 0, 0, 0, 0, 0, 3, 3]) #5s Irradiation
52
53 tetralayer_power = np.array([30.3, 25.4, 22.2, 20.2, 18.2, 16.3])
54 tetralayer_layer_t1 = np.array([0, 0, 0, 4, 4, 4]) #2s Irradiation
55 tetralayer_layer_t2 = np.array([0, 0, 0, 0, 0, 4]) #5s Irradiation
56
57
58 monol_fl, d_monol_fl = transform_power_uncertainty(monolayer_power)
59 bil_fl, d_bil_fl = transform_power_uncertainty(bilayer_power)
60 tril_fl, d_tril_fl = transform_power_uncertainty(trilayer_power)
61 tetral_fl, d_tetral_fl = transform_power_uncertainty(tetralayer_power)
62
63 plt.rcParams.update({
64     'font.size': 12,           # Default font size
65     'axes.titlesize': 15,     # Title size
66     'axes.labelsize': 14,     # X/Y label size
67     'xtick.labelsize': 12,    # Tick label size
68     'ytick.labelsize': 12,
69     'legend.fontsize': 12,
70     'font.family': 'serif',   # Use serif fonts like Times New Roman
71 })
72 # Fluence values and corresponding layers
73 fluence_values = [monol_fl, bil_fl, tril_fl, tetral_fl]
74 fluence_errors = [d_monol_fl, d_bil_fl, d_tril_fl, d_tetral_fl]

```

```

75 layer_counts = [monolayer_layers_t1, bilayer_layers_t1, trilayer_layers_t1,
76                 ↪ tetralayer_layer_t1]
77 # Plotting
78 plt.figure(figsize=(10, 6))
79 labels = ['Monolayer', 'Bilayer', 'Trilayer', 'Tetralayer']
80
81 for fluence, error, layers, label in zip(fluence_values, fluence_errors,
82     ↪ layer_counts, labels):
83     error = 0
84     plt.errorbar(fluence, layers, xerr=error, label=label, fmt='-o', capsize=5)
85
86 # Threshold values for more layers
87 th_layers = np.array([1, 2, 3, 4])
88 th_values_power = np.array([25.5, 22.3, 20.6, 20.2]) #Last value before cut
89     ↪ starting at monolayer
90 th_values, d_th_values = transform_power_uncertainty(th_values_power)
91
92 plt.yticks(range(0, 6, 1))
93 plt.xlabel('Fluence (mJ/cm^2)')
94 plt.ylabel('Number of Layers')
95 plt.title('Number of Layers after 2s Laser Irradiation')
96 plt.legend()
97 plt.grid(True)
98 plt.show()
99
100 from sklearn.metrics import mean_squared_error
101 # Different Fits
102 def fit_fl_th(N, C0, p): #Fit without saturation
103     return C0*(N**-p)
104
105 def fit_inverse_alpha(N, c, k, alpha): #Fit general invers
106     return c+k*(N**alpha)
107
108 def fit_inverse(N, c, k): #Fit 1/N
109     return c+k/N
110
111 params, covariance = curve_fit(fit_fl_th, th_layers, th_values, p0=(0.8, 2))
112 c0_fit, p_fit = params
113
114 params2, covariance2 = curve_fit(fit_inverse_alpha, th_layers, th_values, p0=(12,
115     ↪ 4, -1))
116 c_fit, k_fit, alpha_fit = params2
117 param_errors = np.sqrt(np.diag(covariance2))
118
119 params3, covariance3 = curve_fit(fit_inverse, th_layers, th_values, p0=(12, 4))
120 c_2fit, k_2fit= params3
121
122 # Fit berechnen
123 x_fit = np.linspace(min(th_layers), max(th_layers+2))
124
125 # Predict on original data points (for MSE)
126 y_pred_fl_th = fit_fl_th(th_layers, c0_fit, p_fit)
127 y_pred_inverse_alpha = fit_inverse_alpha(th_layers, c_fit, k_fit, alpha_fit)
128 y_pred_inverse = fit_inverse(th_layers, c_2fit, k_2fit)
129
130 # MSE calculation (Error for each fit)
131 mse_fl_th = mean_squared_error(th_values, y_pred_fl_th)
132 mse_inverse_alpha = mean_squared_error(th_values, y_pred_inverse_alpha)
133 mse_inverse = mean_squared_error(th_values, y_pred_inverse)
134
135 # Print MSEs
136 print(f"MSE (Power Law fit): {mse_fl_th:.4f}")
137 print(f"MSE (Inverse Alpha fit): {mse_inverse_alpha:.4f}")
138 print(f"MSE (Inverse fit): {mse_inverse:.4f}")
139
140 # Fit plotting range
141 x_fit = np.linspace(min(th_layers), max(th_layers + 2))
142 y_fit = fit_fl_th(x_fit, c0_fit, p_fit)
143 y_inverse_alpha_fit = fit_inverse_alpha(x_fit, c_fit, k_fit, alpha_fit)
144 y_inverse_fit = fit_inverse(x_fit, c_2fit, k_2fit)

```

```

144 plt.figure(figsize=(10, 6))
145
146
147 plt.errorbar(th_layers, th_values, yerr=d_th_values, fmt='o', capsize=5,
    ↪ label='Data', color='red')
148 #plt.plot(x_fit, y_fit, label=f'Fit: y = c0*N^-p, c0={c0_fit:.2f}, p={p_fit:.2f}')
149 plt.plot(x_fit, y_inverse_alpha_fit, label=f'Fit: y = c+kx^a, with c={c_fit:.2f},
    ↪ k={k_fit:.2f}, a={alpha_fit:.2f}', linestyle='-')
150 #plt.plot(x_fit, y_inverse_fit, label=f'Fit: y = c+k/x, with c={c_2fit:.2f},
    ↪ k={k_2fit:.2f}', linestyle='-')
151
152 plt.xlabel('Number of Layers')
153 plt.ylabel('Threshold Fluence (mJ/cm^2)')
154 plt.title('Damage Threshold (Fluence) Depending on Number of Layers')
155 plt.legend()
156 plt.grid(True)
157 plt.show()
158
159 print(f"Fit Parameters: c0={c0_fit:.2f}, p={p_fit:.2f}")
160 print(f"Fit Parameters (Inverse Alpha): c={c_fit:.2f} pm {param_errors[0]:.2f},
    ↪ k={k_fit:.2f} pm {param_errors[1]:.2f}, alpha={alpha_fit:.2f} pm
    ↪ {param_errors[2]:.2f}")

```

A.0.4 Python Script for Time-Dependent Threshold

In addition to the part of the script from the previous section where the functions are defined and the data is stored, the part for the time-dependent threshold

```

1 #Time to amount of pulses
2 pulses_t1 = 2*freq
3 pulses_t2 = 5*freq
4 pulses_t3 = 8*freq
5
6 th_monolayer_power = np.array([25.5, 21.0, 20.4])
7 th_bilayer_power = np.array([22.3, 18.1])
8 th_trilayer_power = np.array([20.6, 16.2])
9 th_tetralayer_power = np.array([20.2, 16.3])
10
11 th_monolayer = transform_power_uncertainty(th_monolayer_power)
12 th_bilayer = transform_power_uncertainty(th_bilayer_power)
13 th_trilayer = transform_power_uncertainty(th_trilayer_power)
14 th_tetralayer = transform_power_uncertainty(th_tetralayer_power)
15
16 pulses_monolayer = np.array([pulses_t1, pulses_t2, pulses_t3])
17 pulses_multilayer = np.array([pulses_t1, pulses_t2])
18
19 # Plotting
20 plt.figure(figsize=(10, 6))
21 plt.errorbar(th_monolayer[0], pulses_monolayer, xerr=th_monolayer[1],
    ↪ label='monolayers', fmt='-o', capsize=5)
22 plt.errorbar(th_bilayer[0], pulses_multilayer, xerr=th_bilayer[1],
    ↪ label='bilayers', fmt='-o', capsize=5)
23 plt.errorbar(th_trilayer[0], pulses_multilayer, xerr=th_trilayer[1],
    ↪ label='trilayers', fmt='-o', capsize=5)
24 plt.errorbar(th_tetralayer[0], pulses_multilayer, xerr=th_tetralayer[1],
    ↪ label='tetralayers', fmt='-o', capsize=5)
25
26 #Fitting
27 def fit_pulses_th(f1, th, s):
28     return (f1/th)**(1/(s-1))
29
30 lower_bounds = [100, 0.7]
31 upper_bounds = [180, 1.0]
32
33 params, covariance = curve_fit(fit_pulses_th, th_monolayer[0], pulses_monolayer,
    ↪ p0=(140, 0.88))
34 th_fit, s_fit = params
35 param_errors = np.sqrt(np.diag(covariance))
36

```

```

37 x_fit = np.linspace(min(th_monolayer[0]-1), max(th_monolayer[0]+2), 200)
38 y_fit = fit_pulses_th(x_fit, th_fit, s_fit)
39 plt.plot(x_fit, y_fit, label=f'Fit y = (x/F_0)^(1/s-1): F_0={th_fit:.2f},
    ↪ s={s_fit:.2f}')
40
41 print(f"Fitted parameters: F_0 = {th_fit:.2f} pm {param_errors[0]:.2f}, s =
    ↪ {s_fit:.2f} pm {param_errors[1]:.2f}")
42
43 plt.xlabel('Fluence (mJ/cm^2)')
44 plt.ylabel('Number of Pulses')
45 plt.title('Number of Pulses to Damage for certain Fluence (Few Layers)')
46 plt.legend()
47 plt.grid(True)
48 plt.show()
49 # Oberer Fit (f + df)
50 params_max, _ = curve_fit(fit_pulses_th, th_monolayer[0]+th_monolayer[1],
    ↪ pulses_monolayer, p0=(140, 0.88))
51 f0_max, s_max = params_max
52
53 # Unterer Fit (f - df)
54 params_min, _ = curve_fit(fit_pulses_th, th_monolayer[0]-th_monolayer[1],
    ↪ pulses_monolayer, p0=(140, 0.88))
55 f0_min, s_min = params_min
56
57 # Fehlerabschätzung
58 f0_err = (f0_max - f0_min) / 2
59 s_err = (s_max - s_min) / 2
60
61 # Ausgabe
62 print(f"f_0 = {th_fit:.2f}      {f0_err:.2f}")
63 print(f"s = {s_fit:.2f}      {s_err:.2f}")
64
65
66 six_layer_power = np.array([34, 35.5, 38.0, 39.4, 40.2, 42.3])
67 six_layer_time = np.array([70, 54, 22, 14, 7, 7])
68
69 eight_layer_power = np.array([33.6, 36.8, 39, 41.1])
70 eight_layer_time = np.array([60, 24, 13, 4])
71
72 nine_layer_power = np.array([33.4, 36.2, 38.3, 39.8, 42.3])
73 nine_layer_time = np.array([60, 24, 12, 6, 5])
74
75 ten_layer_power = np.array([34, 35.8, 38.8, 40.4, 41.8])
76 ten_layer_time = np.array([43, 25, 10, 6, 6])
77
78
79 sixl_fluence, d_sixl_fl = transform_power_uncertainty(six_layer_power)
80 eightl_fluence, d_eightl_fl = transform_power_uncertainty(eight_layer_power)
81 ninel_fluence, d_ninel_fl = transform_power_uncertainty(nine_layer_power)
82 tenl_fluence, d_tenl_fl = transform_power_uncertainty(ten_layer_power)
83
84 sixl_fluence = sixl_fluence*0.43
85 eightl_fluence = eightl_fluence*0.43
86 ninel_fluence = ninel_fluence*0.43
87 tenl_fluence = tenl_fluence*0.43
88
89 d_eightl_fl = d_eightl_fl*0.43
90 d_ninel_fl = d_ninel_fl*0.43
91
92 sixl_pulses = six_layer_time * freq
93 eightl_pulses = eight_layer_time * freq
94 ninel_pulses = nine_layer_time * freq
95 tenl_pulses = ten_layer_time * freq
96
97 # Plotting
98 plt.figure(figsize=(10, 6))
99 plt.errorbar(sixl_fluence, sixl_pulses, yerr=freq, label='six layers', fmt='o',
    ↪ capsizes=5)
100 plt.errorbar(eightl_fluence, eightl_pulses, yerr=freq, label='eight layers',
    ↪ fmt='o', capsizes=5)
101 plt.errorbar(ninel_fluence, ninel_pulses, yerr=freq, label='nine layers', fmt='o',
    ↪ capsizes=5)
102 plt.errorbar(tenl_fluence, tenl_pulses, yerr=freq, label='ten layers', fmt='o',

```

```

    ↪ capsize=5)
103 #Fitting
104 def fit_time_th(fl, th, s):
105     return (fl/th)**(1/(s-1))
106
107 sixl_params, sixl_covariance = curve_fit(fit_time_th, sixl_fluence, sixl_pulses,
    ↪ p0=(140, 0.88))
108 sixl_th_fit, sixl_s_fit = sixl_params
109 sixl_param_errors = np.sqrt(np.diag(sixl_covariance))
110 sixl_x_fit = np.linspace(min(sixl_fluence), max(sixl_fluence+1), 200)
111 sixl_y_fit = fit_time_th(sixl_x_fit, sixl_th_fit, sixl_s_fit)
112 plt.plot(sixl_x_fit, sixl_y_fit, label=f'Fit 6-layers: F_0={sixl_th_fit:.3f},
    ↪ s={sixl_s_fit:.3f}', color="blue")
113
114 eightl_params, eightl_covariance = curve_fit(fit_time_th, eightl_fluence,
    ↪ eightl_pulses, p0=(140, 0.88))
115 eightl_th_fit, eightl_s_fit = eightl_params
116 eightl_param_errors = np.sqrt(np.diag(eightl_covariance))
117 eightl_x_fit = np.linspace(min(eightl_fluence), max(eightl_fluence+2), 200)
118 eightl_y_fit = fit_time_th(eightl_x_fit, eightl_th_fit, eightl_s_fit)
119 plt.plot(eightl_x_fit, eightl_y_fit, label=f'Fit 8-layers:
    ↪ F_0={eightl_th_fit:.3f}, s={eightl_s_fit:.3f}', color='orange')
120
121 ninel_params, ninel_covariance = curve_fit(fit_time_th, ninel_fluence,
    ↪ ninel_pulses, p0=(140, 0.88))
122 ninel_th_fit, ninel_s_fit = ninel_params
123 ninel_param_errors = np.sqrt(np.diag(ninel_covariance))
124 ninel_x_fit = np.linspace(min(ninel_fluence), max(ninel_fluence+2), 200)
125 ninel_y_fit = fit_time_th(ninel_x_fit, ninel_th_fit, ninel_s_fit)
126 plt.plot(ninel_x_fit, ninel_y_fit, label=f'Fit 9-layers: F_0={ninel_th_fit:.3f},
    ↪ s={ninel_s_fit:.3f}', color='green')
127
128 tenl_params, tenl_covariance = curve_fit(fit_time_th, tenl_fluence, tenl_pulses,
    ↪ p0=(140, 0.88))
129 tenl_th_fit, tenl_s_fit = tenl_params
130 tenl_param_errors = np.sqrt(np.diag(tenl_covariance))
131 print(tenl_th_fit, tenl_s_fit)
132 tenl_x_fit = np.linspace(min(tenl_fluence), max(tenl_fluence+2), 200)
133 tenl_y_fit = fit_time_th(tenl_x_fit, tenl_th_fit, tenl_s_fit)
134 plt.plot(tenl_x_fit, tenl_y_fit, label=f'Fit 10-layers: F_0={tenl_th_fit:.3f},
    ↪ s={tenl_s_fit:.3f}', color='red')
135
136 plt.xlabel('Fluence (mJ/cm^2)')
137 plt.ylabel('Number of Pulses')
138 plt.title('Number of Pulses to Damage for certain Fluence (Many Layers)')
139 plt.legend()
140
141
142 # Fehlerbalken-Plot
143 plt.figure(figsize=(10, 6))
144 ax = plt.gca()
145 ax.errorbar(ninel_pulses, ninel_fluence, xerr=freq, yerr=d_ninel_fl,
146             label='Nine Layers', fmt='o', capsize=5)
147
148 # Fit-Funktion
149 def fit_pulses_N(N, th, s):
150     return th * (N**(s - 1))
151
152 # Fit
153 params, covariance = curve_fit(fit_pulses_N, ninel_pulses, ninel_fluence, p0=(80,
    ↪ 0.9))
154 th_fit, s_fit = params
155 param_errors = np.sqrt(np.diag(covariance))
156
157 # Fit-Kurve
158 x_fit = np.linspace(min(ninel_pulses) * 0.9, max(ninel_pulses) * 1.1, 200)
159 y_fit = fit_pulses_N(x_fit, th_fit, s_fit)
160 ax.plot(x_fit, y_fit, label=f'Fit: F_0 = {th_fit:.2f} pm {param_errors[0]:.2f}, s
    ↪ = {s_fit:.2f} pm {param_errors[1]:.2f}')
161
162 # Vertical lines for seconds
163 max_pulse = max(x_fit)
164 seconds = np.arange(5, int(max_pulse // freq) + 1, 5)

```

```

165 pulse_marks = seconds * freq
166 for p in pulse_marks:
167     ax.axvline(p, color='gray', linestyle='--', linewidth=0.7, alpha=0.6)
168
169 # Second axis for time
170 def pulses_to_time(x):
171     return x / freq
172
173 def time_to_pulses(t):
174     return t * freq
175
176 secax = ax.secondary_xaxis('top', functions=(pulses_to_time, time_to_pulses))
177 secax.set_xlabel("Time (s)")
178
179 # Achsentitel und Anzeige
180 ax.set_xlabel('Number of Pulses')
181 ax.set_ylabel('Threshold Fluence (mJ/cm^2)')
182 ax.set_title('Damage Threshold (Fluence) on Number of Pulses (Irradiation Time)
183           ↪ for Nine Layers')
184 ax.legend()
185 ax.grid(True)
186
187 plt.tight_layout()
188 plt.show()

```

A.0.5 Python Script for Graphene Cutting Characteristics

```

1     import pandas as pd
2     import matplotlib.pyplot as plt
3     import numpy as np
4     from scipy.optimize import curve_fit
5
6     plt.rcParams.update({
7         'font.size': 12,           # Default font size
8         'axes.titlesize': 15,     # Title size
9         'axes.labelsize': 14,    # X/Y label size
10        'xtick.labelsize': 12,    # Tick label size
11        'ytick.labelsize': 12,
12        'legend.fontsize': 12,
13        'font.family': 'serif',   # Use serif fonts like Times New Roman
14    })
15
16 # Datei einlesen (ab Zeile 4, Leerzeichen als Trennzeichen)
17 df = pd.read_csv("data/analysis_cut_2", delim_whitespace=True, skiprows=3,
18                 ↪ header=None)
19 df.columns = ['x [m]', 'y [m]']
20
21 # Umrechnung der Einheiten
22 df['x [microm]'] = df['x [m]'] * 1e6 # Meter      Mikrometer
23 df['y [nm]'] = df['y [m]'] * 1e9   # Meter      Nanometer
24
25 plt.figure(figsize=(10, 6))
26 plt.plot(df['x [microm]'], df['y [nm]'], linestyle='-')
27
28 # Double-Step-Function
29 def double_step(x, x1, x2, y0, h):
30     return y0 - h * ((x > x1) & (x < x2)).astype(float)
31
32 # Fit-Kurve berechnen
33 x_fit = np.linspace(1.21, 3.42, 500)
34 y_fit = double_step(x_fit, 1.75, 3.07, 0, 0.51)
35
36 x_fit2 = np.linspace(7.4, 10.5, 500)
37 y_fit2 = double_step(x_fit2, 8.17, 9.81, 0.22, 0.57)
38
39 x_fit3 = np.linspace(16, 19, 500)
40 y_fit3 = double_step(x_fit3, 16.72, 18.43, 0.06, 0.61)
41
42 positionen = [ #From Gwyddion Analysis
43               (4.8, -0.4, "Deltax = 1.32 microm\nh = 0.51 nm"),

```

```

43     (11.7, -0.2, "Deltax = 1.64 microm\nh = 0.57 nm"),
44     (20.2, -0.4, "Deltax = 1.71 microm\nh = 0.61 nm"),
45 ]
46
47 # Text in den Plot schreiben
48 for x, y, text in positionen:
49     plt.text(x, y, text,
50             fontsize=12, color='black',
51             ha='center', va='top', # horizontale / vertikale Ausrichtung
52             bbox=dict(boxstyle="round,pad=0.3", fc="white", ec="gray", lw=0.5))
53
54 # Plot erstellen ohne Marker (nur Linie)
55 plt.title('Profile of Graphene Cuts with Double-Step Fit')
56 plt.plot(x_fit, y_fit, label='Double Step Fit', color='red')
57 plt.plot(x_fit2, y_fit2, label='Double Step Fit', color='red')
58 plt.plot(x_fit3, y_fit3, label='Double Step Fit', color='red')
59 plt.xlabel('x (microm)')
60 plt.ylabel('y (nm)')
61 plt.grid(True)
62 plt.tight_layout()
63 plt.show()

```

Appendix B

Commands for Controlling Motors and Laser

Some of the most important ASCII commands to control both the motors and the laser are described below. A complete list of motor commands can be found here: [ESP301 User's Manual](#)

Motion Controller

ASCII Command	Variables	Description
xPAXX	x: Axis; XX: Value	Move to absolute position
xPRXX	x: Axis; XX: Value	Move to relative position
xVAXX	x: Axis; XX: Value	Set velocity. If XX = '?', get current velocity
xACXX	x: Axis; XX: Value	Set acceleration. If XX = '?', get current acceleration
xTP?	x: Axis	Retrieve current axis position
xOR	x: Axis	Move to home position
xST	x: Axis	Stop movement
xMO / xMF	x: Axis	Turn motor ON (MO) / OFF (MF)
AB	–	Abort all operations

Laser Controller

ASCII Command	Variables	Description
sEmission_flagX	X: 0 / 1	Turn laser ON (1) / OFF (0)
gstatus	Returns: bits	Returns bit sequence indicating current laser status (POWER, READY, ON, ERROR)
sRemote_flagX	X: 0 / 1	Enable (1) / Disable (0) Remote (ASCII) control of Laser



Appendix C

Measurements

All measurements concerning the layer-dependent and time-dependent damage thresholds were performed manually, following the procedure described in the results chapter. This appendix shows the raw data acquired.

C.1 Layer-dependent Damage Threshold

C.2 Time-Dependent Damage Threshold

Table C.1: Number of remaining layers after 2 seconds of irradiation at various laser powers (errors not included)

Sample Type	Power (mW)	Fluence (mJ/cm ²)	Remaining Layers
Monolayer	40.0	27.01	0
	35.4	23.90	0
	30.0	20.25	0
	28.1	18.97	0
	25.5	17.22	1
	22.0	14.85	1
	20.1	13.56	1
	18.0	12.15	1
Bilayer	40.4	27.25	0
	35.6	24.03	0
	30.5	20.60	0
	25.7	17.36	0
	22.3	15.06	2
	20.4	13.78	2
	18.1	12.23	2
	16.2	10.94	2
Trilayer	40.0	27.01	0
	35.8	24.16	0
	30.0	20.25	0
	25.2	17.04	0
	22.5	15.19	0
	20.6	13.91	3
	18.8	12.69	3
	16.2	10.94	3
Tetralayer	30.3	20.45	0
	25.4	17.16	0
	22.2	15.02	0
	20.2	13.66	4
	18.2	12.30	4
	16.3	11.02	4

Table C.2: Time-dependent damage threshold: Minimum exposure time and corresponding fluence required to damage flakes of varying thickness

Sample Type	Power (mW)	Fluence (mJ/cm ²)	Time (s)	Pulses ($\cdot 10^8$)
Monolayer	25.5	17.22	2	1
	21.1	14.25	5	2.5
	20.1	13.57	8	4
Bilayer	22.3	15.06	2	1
	18.1	12.22	5	2.5
Trilayer	20.6	13.91	2	1
	16.2	10.94	5	2.5
Tetralayer	20.2	13.66	2	1
	16.3	11.02	5	2.5
6 layers	42.3	12.28	7	3.5
	40.2	11.66	7	3.5
	39.4	11.43	14	7
	38.0	11.02	22	11
	35.5	10.30	54	27
	34.0	9.87	70	35
8 layers	41.1	11.91	4	2
	39.0	11.31	13	6.5
	36.8	10.67	24	12
	33.6	9.76	60	30
9 layers	42.3	12.28	4	2
	39.8	11.54	7	3.5
	38.3	11.11	12	6
	36.2	10.51	24	12
	33.4	9.70	60	30
10 layers	41.8	12.12	6	3
	40.4	11.72	6	3
	38.8	11.26	10	5
	35.8	10.37	25	12.5
	34.0	9.87	43	21.5

Disclaimer of AI Usage

In this work, AI tools (such as **ChatGPT** and **DeepL**) were used to correct spelling and grammar errors, refine the writing style and Python scripts, explain concepts (which were then corroborated with the provided bibliography), and analyze and summarize scientific articles for preliminary analysis.

Bibliography

- [1] S. V. S. Prasad et al. *Introduction, History, and Origin of Two Dimensional (2D) Materials*. 2021.
- [2] D.K. Efetov B.A. Bernevig. “Twisted bilayer graphene’s gallery of phases”. In: *Physics Today* 77.4 (Apr. 2024), pp. 38–44.
- [3] Eric Pop, Vikas Varshney, and Ajit K. Roy. “Thermal properties of graphene: Fundamentals and applications”. In: *MRS Bulletin* 37.12 (2012), pp. 1273–1281. DOI: [10.1557/mrs.2012.203](https://doi.org/10.1557/mrs.2012.203).
- [4] Yuan Cao et al. “Unconventional superconductivity in magic-angle graphene superlattices”. In: *Nature* 556.7699 (2018), pp. 43–50. DOI: [10.1038/nature26160](https://doi.org/10.1038/nature26160). URL: <https://www.nature.com/articles/nature26160>.
- [5] G. Di Battista T. Taniguchi E. Olsson D.K. Efetov J. Díez-Mérida I. Das. “High-yield fabrication of bubble-free magic-angle twisted bilayer graphene devices with high twist-angle homogeneity”. In: *Newton* 1 (Mar. 2025), p. 100007.
- [6] Authors omitted for brevity (from supplementary info). “Flavour Hund’s coupling, Chern gaps and charge diffusivity in moiré graphene”. In: *Nature* (2021). Supplementary Information. URL: <https://doi.org/10.1038/s41586-021-03366-w>.
- [7] Dan Bing et al. “Optical contrast for identifying the thickness of two-dimensional materials”. In: *Optics Communications* 406 (2018), pp. 128–138. DOI: [10.1016/j.optcom.2017.06.012](https://doi.org/10.1016/j.optcom.2017.06.012).
- [8] Kamila K. Mentel et al. “Shaping graphene with optical forging: from a single blister to complex 3D structures”. In: *Nanoscale Advances* 3 (2021), pp. 1431–1442. DOI: [10.1039/D0NA00980A](https://doi.org/10.1039/D0NA00980A).
- [9] S. Dhar et al. “A new route to graphene layers by selective laser ablation”. In: *AIP Advances* 1.2 (Apr. 2011), p. 022109. DOI: [10.1063/1.3584204](https://doi.org/10.1063/1.3584204).
- [10] A. H. Castro Neto et al. “The electronic properties of graphene”. In: *Reviews of Modern Physics* 81.1 (2009), pp. 109–162. DOI: [10.1103/RevModPhys.81.109](https://doi.org/10.1103/RevModPhys.81.109).
- [11] F. Schäffel. “Chapter 2 - The Atomic Structure of Graphene and Its Few-Layer Counterparts”. In: *Graphene*. Ed. by J. H. Warner et al. Elsevier, 2013, pp. 5–12.
- [12] Justin George and Debes Bhattacharyya. “Graphene: an introduction”. In: *Recent Advances in Graphene and Graphene-Based Technologies*. IOP Publishing, 2023. Chap. 1, pp. 1–26. DOI: [10.1088/978-0-7503-3999-5ch1](https://doi.org/10.1088/978-0-7503-3999-5ch1).

- [13] Wikipedia contributors. *Electronic Properties of Graphene* — *Wikipedia, The Free Encyclopedia*. 2025. URL: https://en.wikipedia.org/wiki/Electronic_properties_of_graphene (visited on 06/04/2025).
- [14] J. H. Warner et al. “Chapter 3 - Properties of Graphene”. In: *Graphene*. Ed. by J. H. Warner et al. Elsevier, 2013, pp. 62–64.
- [15] Dmitri Efetov. *Lecture 2: Introduction to Graphene and 2D Materials*. Summer Semester 2025. May 5, 2025. URL: <https://www.physik.lmu.de/en/chairs/efetov/teaching/index.html>.
- [16] Deblina Das and Swapan K. Pati. “CVD Growth, Characterization and Applications of Transition Metal Dichalcogenide Nanosheets”. In: *Recent Advances in Nanomaterials*. Ed. by Pooja Ghosh and Keka Sarkar. Springer, Cham, 2021, pp. 135–155. DOI: [10.1007/978-3-030-80323-0_7](https://doi.org/10.1007/978-3-030-80323-0_7).
- [17] Egor P. Sharin and Roman S. Tihonov. “Two-dimensional carbon structures study within density functional theory”. In: *AIP Conference Proceedings* 1907.1 (2017), p. 030028. DOI: [10.1063/1.5012650](https://doi.org/10.1063/1.5012650).
- [18] L. Menacho, M. Carrasco, and Z. Ayala. “Comparison between monolayer and bilayer graphene energy bands using the Tight Binding model”. In: *Journal of Physics: Conference Series*. Vol. 1143. 2018, p. 012022. DOI: [10.1088/1742-6596/1143/1/012022](https://doi.org/10.1088/1742-6596/1143/1/012022).
- [19] Rafi Bistritzer and Allan H. MacDonald. “Moiré bands in twisted double-layer graphene”. In: *Proceedings of the National Academy of Sciences of the United States of America* 108.30 (2011), pp. 12233–12237. DOI: [10.1073/pnas.1108174108](https://doi.org/10.1073/pnas.1108174108).
- [20] Ruizhi Wang. *Laser Ablation of Graphene: Fundamental Processes and Applications*. Master Thesis, ETH Zurich, accessed 2025-06-04. ETH Zurich. 2013. URL: <https://doi.org/10.3929/ethz-a-010089121>.
- [21] R. R. Nair et al. “Fine Structure Constant Defines Visual Transparency of Graphene”. In: *Science* 320.5881 (2008), p. 1308. DOI: [10.1126/science.1156965](https://doi.org/10.1126/science.1156965).
- [22] Zhiyong Wei et al. “In-plane lattice thermal conductivities of multilayer graphene films”. In: *Carbon* 49.8 (Feb. 2011), pp. 2653–2658. DOI: [10.1016/j.carbon.2011.02.051](https://doi.org/10.1016/j.carbon.2011.02.051).
- [23] Tianqi Dong et al. “Evaluating femtosecond laser ablation of graphene on SiO₂/Si substrate”. In: *Journal of Laser Applications* 28.2 (Mar. 2016), p. 022202. DOI: [10.2351/1.4944510](https://doi.org/10.2351/1.4944510).
- [24] Valter Kiisk et al. “Nanosecond laser treatment of graphene”. In: *Applied Surface Science* 276 (2013), pp. 133–137. DOI: [10.1016/j.apsusc.2013.03.047](https://doi.org/10.1016/j.apsusc.2013.03.047).
- [25] M. Gai X. Huang L. Liu Y. Huang H. Yu J. Bian. “Comparative study of laser-induced graphene fabricated in atmospheric and interface-confined environments”. In: *Applied Surface Science* 673 (Aug. 2024), p. 160889.
- [26] A. Gil-Villalba et al. “Deviation from threshold model in ultrafast laser ablation of graphene at sub-micron scale”. In: *Applied Physics Letters* 107.6 (Aug. 2015), p. 061103. DOI: [10.1063/1.4928391](https://doi.org/10.1063/1.4928391).

- [27] S. Ghosh et al. “Extremely high thermal conductivity of graphene: Prospects for thermal management applications in nanoelectronic circuits”. In: *Applied Physics Letters* 92 (Apr. 2008), p. 151911. DOI: [10.1063/1.2907977](https://doi.org/10.1063/1.2907977).
- [28] L. Lindsay, D. A. Broido, and N. Mingo. “Flexural phonons and thermal transport in graphene”. In: *Physical Review B* 82.11 (2010), p. 115427. DOI: [10.1103/PhysRevB.82.115427](https://doi.org/10.1103/PhysRevB.82.115427).
- [29] Thomas Greber. “Graphene and Boron Nitride Single Layers”. In: *Handbook of Nanophysics*. Ed. by Klaus Sattler. arXiv:0904.1520 [cond-mat.mtrl-sci]. Taylor and Francis Books, Inc., 2009. URL: <https://arxiv.org/abs/0904.1520>.
- [30] Matthew Yankowitz et al. “van der Waals heterostructures combining graphene and hexagonal boron nitride”. In: *Nature Reviews Physics* 1 (2019), pp. 112–125. DOI: [10.1038/s42254-018-0016-0](https://doi.org/10.1038/s42254-018-0016-0).
- [31] A. K. Geim and I. V. Grigorieva. “Van der Waals heterostructures”. In: *Nature* 499 (2013), pp. 419–425. DOI: [10.1038/nature12385](https://doi.org/10.1038/nature12385).
- [32] Dmitri K. Efetov and Philip Kim. “Controlling Electron-Phonon Interactions in Graphene at Ultrahigh Carrier Densities”. In: *Physical Review Letters* 105.25 (2010), p. 256805. DOI: [10.1103/PhysRevLett.105.256805](https://doi.org/10.1103/PhysRevLett.105.256805).
- [33] C. R. Dean et al. “Boron nitride substrates for high-quality graphene electronics”. In: *Nature Nanotechnology* 5.10 (2010), pp. 722–726. DOI: [10.1038/nnano.2010.172](https://doi.org/10.1038/nnano.2010.172).
- [34] Wikipedia contributors. *Laser — Wikipedia, The Free Encyclopedia*. 2025. URL: <https://en.wikipedia.org/wiki/Laser> (visited on 06/04/2025).
- [35] John F. Ready and David F. Farson. “LIA Handbook of Laser Materials Processing”. In: *Laser Fundamentals*. 1st. 715 pages. Orlando, FL: Laser Institute of America, 2001.
- [36] LibreTexts Contributors. *15.3: Two-Level Systems Cannot Form Population Inversions*. 2020. URL: https://chem.libretexts.org/Courses/BethuneCookman_University/BCU%3A_CH_332_Physical_Chemistry_II/Text/15%3A_Lasers_Laser_Spectroscopy_and_Photochemistry/15.3%3A_Two-Level_Systems_Cannot_Form_Population_Inversions (visited on 06/04/2025).
- [37] Eurico Assuncao and Stewart Williams. “Comparison of continuous wave and pulsed wave laser welding effects”. In: *Optics and Lasers in Engineering* 51.6 (2013), pp. 674–680. DOI: [10.1016/j.optlaseng.2013.01.007](https://doi.org/10.1016/j.optlaseng.2013.01.007).
- [38] Alejandro Tur et al. “Minimization of the thermal material effects on pulsed dynamic laser welding”. In: *Journal of Materials Processing Technology* 246 (2017), pp. 13–21. DOI: [10.1016/j.jmatprotec.2017.03.007](https://doi.org/10.1016/j.jmatprotec.2017.03.007).
- [39] MeetOptics Academy. *Pulsed Lasers*. Accessed: 2025-06-11. 2025.
- [40] Newport Corporation. *Average and Peak Power Calculations for Pulsed Lasers*. n.d. URL: https://www.newport.com/medias/sys_master/images/images/h8f/h7a/8797052108830/Average-and-Peak-Power-Calculation-Tech-Note-1.pdf (visited on 06/04/2025).

- [41] Thorlabs, Inc. *Laser Pulses: Power, Energy, and Related Equations*. n.d. URL: https://www.thorlabs.com/images/tabimages/Laser_Pulses_Power_Energy_Equations.pdf (visited on 06/04/2025).
- [42] Encyclopædia Britannica. *The Compound Microscope*. n.d. URL: <https://www.britannica.com/technology/microscope/The-compound-microscope> (visited on 06/04/2025).
- [43] Microscope World. *Infinity Corrected Optics*. n.d. URL: https://www.microscopeworld.com/t-infinity_corrected_optics.aspx (visited on 06/04/2025).
- [44] Evident Scientific. *Basic Knowledge about Microscope Objectives*. n.d. URL: <https://evidentscientific.com/en/learn/microscope/terms/feature15> (visited on 06/04/2025).
- [45] Leica Microsystems. *Microscope Resolution: Concepts, Factors and Calculation*. n.d. URL: <https://www.leica-microsystems.com/science-lab/life-science/microscope-resolution-concepts-factors-and-calculation/> (visited on 06/04/2025).
- [46] Wikipedia contributors. *Diffraction-limited system* — *Wikipedia, The Free Encyclopedia*. 2025. URL: https://en.wikipedia.org/wiki/Diffraction-limited_system (visited on 06/04/2025).
- [47] RP Photonics Encyclopedia. *Dichroic Mirrors*. n.d. URL: https://www.rp-photonics.com/dichroic_mirrors.html (visited on 06/04/2025).
- [48] FindLight Blog. *Dichroic Mirrors Explained: A Comprehensive Guide*. n.d. URL: <https://www.findlight.net/blog/dichroic-mirrors-explained-a-comprehensive-guide/> (visited on 06/04/2025).
- [49] RP Photonics Encyclopedia. *Beam Collimators*. n.d. URL: https://www.rp-photonics.com/beam_collimators.html (visited on 06/04/2025).
- [50] RP Photonics Encyclopedia. *Fiber Collimators*. n.d. URL: https://www.rp-photonics.com/fiber_collimators.html (visited on 06/04/2025).
- [51] Schäfter + Kirchhoff GmbH. *How to Calculate the Collimated Beam Diameter for Single-Mode Fibers*. n.d. URL: <https://www.sukhamburg.com/support/technotes/fiberoptics/coupling/collimatingsm/diameter.html> (visited on 06/04/2025).
- [52] Z. H. Ni et al. “Graphene Thickness Determination Using Reflection and Contrast Spectroscopy”. In: *Nano Letters* 7.9 (2007), pp. 2758–2763. DOI: [10.1021/nl1071254m](https://doi.org/10.1021/nl1071254m).
- [53] P. Blake et al. “Making graphene visible”. In: *Applied Physics Letters* 91 (June 2007).
- [54] Z.B. Wang A.A. Pena D.J. Whitehead M.L. Zhong Z. Lin-H.W. Zhu W. Zhang L. Li. “Ti:sapphire femtosecond laser direct micro-cutting and profiling of graphene”. In: *Applied Physics A* 109.2 (July 2012), pp. 291–297.
- [55] NPI Lasers. *Rainbow 1064 OEM Ultrafast Laser*. n.d. URL: http://en.npilasers.com/product/Rainbow_1064_OEM.html (visited on 06/04/2025).
- [56] Spach Optics. *Olympus LCPLN50XIR Near-IR Objective (1-U2M450)*. n.d. URL: <https://www.spachoptics.com/Olympus-LCPLN50XIR-Near-IR-Objective-1-U2M450-p/olympus-lcpln50xir.htm> (visited on 06/04/2025).

- [57] Mitutoyo Corporation. *Microscope Unit 378-505*. n.d. URL: [https://shop.mitutoyo.de/web/mitutoyo/en_DE/mitutoyo/05.03.09c/Microscope%20Unit/\\$catalogue/mitutoyoData/PR/378-505/index.xhtml](https://shop.mitutoyo.de/web/mitutoyo/en_DE/mitutoyo/05.03.09c/Microscope%20Unit/$catalogue/mitutoyoData/PR/378-505/index.xhtml) (visited on 06/04/2025).
- [58] Thorlabs, Inc. *Optical Filters Guide*. n.d. URL: https://www.thorlabs.com/navigation.cfm?guide_id=2005 (visited on 06/04/2025).
- [59] Edmund Optics. *850nm 25.2 x 35.6mm Dichroic Shortpass Filter*. n.d. URL: <https://www.edmundoptics.com/p/850nm-252-x-356mm-dichroic-shortpass-filter/23561/> (visited on 06/04/2025).
- [60] Thorlabs, Inc. *F280APC-1064 Fiber Collimator, FC/APC, 1064 nm, Effective Focal Length 18.4 mm*. n.d. URL: https://www.thorlabs.com/newgrouppage9.cfm?objectgroup_id=1696&pn=F280APC-1064 (visited on 06/04/2025).
- [61] Newport Corporation. *ESP301-3G 3-Axis Motion Controller/Driver, GPIB*. n.d. URL: <https://www.newport.com/p/ESP301-3G> (visited on 06/04/2025).
- [62] hacker-fab. *AmScope Camera Utilities*. GitHub repository. n.d. URL: <https://github.com/hacker-fab/amscope-camera> (visited on 06/04/2025).
- [63] Ivan I. Bobrinetskiy et al. “Ultrafast laser patterning of graphene”. In: *SPIE Microtechnologies* 10248 (2017), p. 1024812. DOI: [10.1117/12.2265430](https://doi.org/10.1117/12.2265430).
- [64] Ayrat Dimiev et al. “Layer-by-Layer Removal of Graphene for Device Patterning”. In: *Science* 331.6021 (2011), pp. 1168–1171. DOI: [10.1126/science.1199183](https://doi.org/10.1126/science.1199183).
- [65] Labster Theory. *Malus’ Law*. n.d. URL: <https://theory.labster.com/malus-law/> (visited on 06/04/2025).
- [66] D. Kim S.J. Lee W. Choi S.J. Kwon J.-H. Han E.-S. Cho H.S. Ryu H.-S. Kim. “Understanding of the mechanism for laser ablation-assisted patterning of graphene/ITO double layers: Role of effective thermal energy transfer”. In: *Micromachines* 11.9 (Aug. 2020), p. 821.
- [67] S.S. Verbridge I.W. Frank D.M. Tanenbaum J.M. Parpia-H.G. Craighead P.L. McEuen J.S. Bunch A.M. van der Zande. “Electromechanical resonators from graphene sheets”. In: *Science* 315.5811 (Jan. 2007), pp. 490–493.
- [68] Wenhui Zhu et al. “Thermal conductivity of amorphous SiO₂ thin film: A molecular dynamics study”. In: *Scientific Reports* 8 (2018), p. 10537. DOI: [10.1038/s41598-018-28925-6](https://doi.org/10.1038/s41598-018-28925-6).
- [69] Zhanliang Sun, Matthias Lenzner, and Wolfgang Rudolph. “Generic incubation law for laser damage and ablation thresholds”. In: *Journal of Applied Physics* 117.7 (Feb. 2015), p. 073102. DOI: [10.1063/1.4913282](https://doi.org/10.1063/1.4913282).

Declaration of Authorship

I hereby declare that this thesis is my own work and I have not used any sources and aids other than those stated in the thesis.

Hiermit erkläre ich, die vorliegende Arbeit selbständig verfasst zu haben und keine anderen als die in der Arbeit angegebenen Quellen und Hilfsmittel benutzt zu haben.

München, 16 June, 2025

Carlos Steiner Navarro

Ludwig-Maximilians-Universität-München

